J. Fluid Mech. (2007), *vol.* 584, *pp.* 301–335.
doi:10.1017/S002211200700674X Printed in the United Kingdom

Velocity and vorticity in weakly compressible isotropic turbulence under longitudinal expansive straining

SAVVAS XANTHOS, MINWEI GONG AND YIANNIS ANDREOPOULOS

Experimental Aerodynamics and Fluid Mechanics Laboratory, The City College of the City University of New York, NY 10031, USA

(Received 2 September 2006 and in revised form 31 March 2007)

The response of homogeneous and isotropic turbulence to streamwise straining action provided by planar expansion waves has been studied experimentally in the CCNY shock tube research facility at several Reynolds numbers. The reflection of a propagating shock wave at the open endwall of the shock tube generated an expansion fan travelling upstream and interacting with the induced flow behind the incident shock wave which has gone through a turbulence generating grid.

A custom-made hot-wire vorticity probe was designed and developed capable of measuring the time-dependent highly fluctuating three-dimensional velocity and vorticity vectors, and associated total temperature, in non-isothermal and inhomogeneous flows with reasonable spatial and temporal resolution. These measurements allowed the computations of the vorticity stretching/tilting terms, vorticity generation through dilatation terms, full dissipation rate of kinetic energy term and full rate-of-strain tensor. The longitudinal size of the straining zone was substantial so that measurements within it were possible. The flow accelerated from a Mach number of 0.23 to about 0.56, a value which is more than twice the initial one.

Although the average value of the applied straining was only between $S_{11} = 130\,\mathrm{s}^{-1}$ and $S_{11} = 240\,\mathrm{s}^{-1}$ and the gradient Mach number was no more than 0.226, the amplitude of fluctuations of the strain rate S_{11} were of the order of $4000\,\mathrm{s}^{-1}$ before the application of straining and were reduced by about 2.5 times downstream of the interaction. This characteristic of high-amplitude bursts and the intermittent behaviour of the flow play a significant role in the dynamics of turbulence.

One of the most remarkable features of the suppression of turbulence is that this process peaks shortly after the application of the straining where the pressure gradient is substantial. It was also found that the total enthalpy variation follows very closely the temporal gradient of pressure within the straining region and peaks at the same location as the pressure gradient.

Attenuation of longitudinal velocity fluctuations has been observed in all experiments. It appears that this attenuation depends strongly on the characteristics of the incoming turbulence for a given straining strength and flow Mach number. The present results clearly show that in most of the cases, attenuation occurs at large times or distances from the turbulence generating grids where length scales of the incoming flow are high and turbulence intensities are low. Thus, large eddies with low-velocity fluctuations are affected the most by the interaction with the expansion waves. Spectral analysis has indicated that attenuation of fluctuations is not the same across all wavenumbers of the spectrum. The magnitude of attenuation appears to be higher in cases of finer mesh grids.

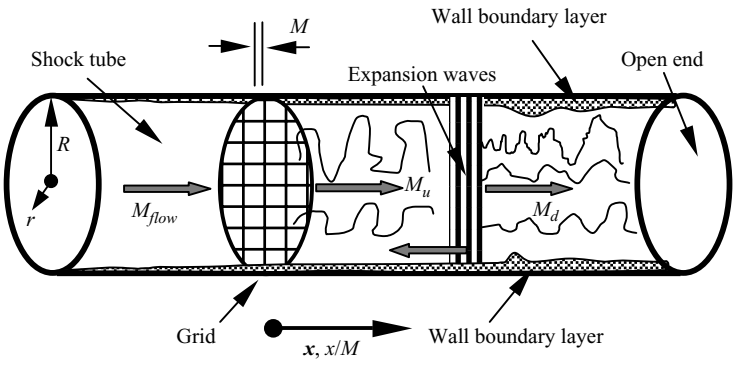

FIGURE 1. Schematic of flow interaction with expansion waves.

1. Introduction

Several investigators (Sternberg 1954; Vivekanandan 1963; Viswanath & Narashima 1973; Narashima & Viswanath 1975; Morkovin 1955; Johnson 1993) have provided direct or indirect evidence demonstrating that in supersonic flow past an expansion corner, the boundary layer reverts from a turbulent state upstream of the corner to a laminar state downstream. This indicates that expansion regions may suppress the level of turbulence activity within a compressible boundary layer completely. This is not unexpected since the boundary layer after the expansion corner encounters a favourable pressure gradient and a strong dilatation effect. Streamline curvature over the convex corner also contributes to a significant reduction in turbulence. This substantial reduction in turbulence can lead to relaminarization of the flow field. Narasimha & Viswanath (1975) attempted to identify a criterion for the occurrence of such reversion, following the theoretical work of Narasimha & Sreenivasan (1973) performed at low speeds, which uses the ratio of the pressure gradient to a characteristic Reynolds stress gradient as the parameter governing the completion of reversion.

Dussauge & Gaviglio (1987) studied the rapid expansion of a turbulent boundary layer in supersonic flow both analytically, based on the rapid distortion theory of Hunt (1973) and experimentally, concentrating on the effect of bulk dilatation on turbulent fluctuations. The authors indicated that their Mach 1.76 turbulent boundary layer had been relaminarized by the expansion. Following the same hypothesis as the previously mentioned authors, Smith & Smits (1991) used the rapid distortion approximation (RDA) to simplify the Reynolds stress equations, retaining terms, which were then modelled as functions of the Reynolds stress tensor and gradients of the mean flow.

Arnette, Samimy & Elliot (1995) and Dawson, Samimy & Arnette (1994) provided more detailed information on the structure of turbulent boundary layers through expansion corners.

In the present work, the straining of isotropic and homogeneous turbulence in the longitudinal direction through an interaction with moving expansion waves (figure 1) has been studied experimentally in our shock-tube facility. In all experiments, the main objective has been to obtain a better understanding of the physics of the interactions and to establish the behaviour of the vorticity field.

Some of the fundamental aspects of turbulence can be studied better in flow configurations where the flow is nearly homogeneous and turbulence is nearly isotropic, where no turbulence is produced and the geometry of the flow is reasonably simplified.

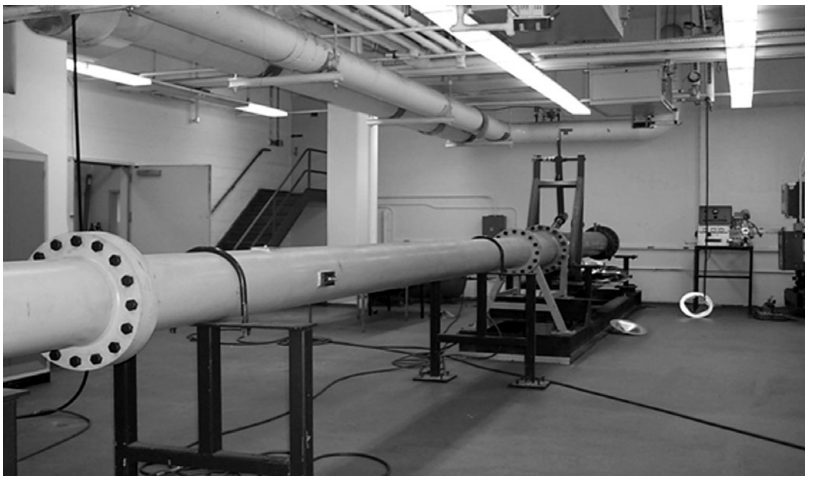

FIGURE 2. Shock tube facility at CCNY.

The presence of a solid wall as a boundary in turbulent flows complicates understanding by introducing large mean velocity gradients at the wall which are responsible for the continuous production of turbulence. Better understanding of the effects of expansion waves on turbulence, can be obtained by considering their interaction with grid-generated turbulence where no streamline curvature and a wall with no-slip conditions are present. The flow behind a turbulence-generating grid contains a large variety of turbulent scales, the size of which depends on the distance from the grid and on its mesh size.

An attempt has been made to measure vorticity in the present flow. Vorticity is a quantity that can describe viscous effects in the absence of baroclinic effects in a flow field, much better than velocity, and it is well suited for defining and identifying organized structures in time-dependent vortical flows because the streamlines and pathlines are completely different in two different inertial frames of reference. In that respect, better understanding of the nature of turbulent structures and vortical motions of turbulent flows, particularly in the high-wavenumber region, often requires spatially and temporally resolved measurements of velocity derivatives.

2. Experimental set-up and techniques

The interactions have been investigated experimentally in the CCNY shock tube facility (figure 2). The shock tube facility is of large-scale dimensions with an inside diameter of 12 in (304 mm) and total length of 90 ft (27.4 m) including all components. The present shock tube facility has three distinguishing features. The most significant one is the ability to control the strength of the reflected shock and the flow quality behind it by using a removable porous endwall, placed at the flange between the dump tank and the working section. The impact of shock wave on the endwall would result in a full normal shock reflection in the case of zero porosity (solid wall), a weak shock reflection in the case of moderate porosity, or expansion waves in the case of 100 % porosity (open endwall). The second feature of the facility is the ability to vary the total length of the driven section by adding or removing one of the several pieces or modules that are available, or rearranging their layout. Proper arrangement of the layout of the various modules of the shock tube can maximize the duration

of the useful flow. The third feature of the facility is its large diameter, which allows for a large area of uniform flow in the absence of wall effects to be available while providing a platform for high spatial resolution in the measurements of turbulence.

The working (test) section is fitted with several hot-wire and pressure ports. Thus, pressure, velocity and temperature data can be acquired simultaneously at various locations downstream from the grid, and therefore reduce the variance between measurements. High-frequency pressure transducers, hot-wire anemometry and Rayleigh-scattering techniques for flow visualization have been used in the present investigation.

A turbulence-generating grid installed in the beginning of the working section of the facility was used to generate a homogeneous and isotropic turbulent flow. The interaction of this flow with expansion waves was produced by using an open endwall.

In order to identify correctly the duration of the useful flow as well as the location of the true expansion wave – turbulence interaction, a predictive tool was developed based on the predictor–corrector total variation diminishing (TVD) scheme. The TVD scheme is an explicit Eulerian finite-difference upwind scheme and an extension of the Roe (1981) scheme to second-order accuracy in space and time. The advantage of the TVD algorithm is that a code based on it is simple, fast, and yet performs well. It is widely used in describing wave motions and patterns in shock tubes. The length of the shock tube has been discretized into 100 intervals and the time step has been controlled by the Courant–Friedrichs–Lewy number. These simulations indicated the existence of two regions of travelling expansion waves. The first one is generated immediately after the rupture of the diaphragm and travels in the opposite direction to that of the shock wave. It is reflected over the endwall of the driver section and then it travels in the same direction as the incident shock wave at a much higher speed owing to the already induced flow. The second system of expansion waves is generated at the open end of the driven section when the incident shock reflects over the open end of the shock tube's working section where the pressure is atmospheric. This system of expansion waves has been used in the present experiments to interact with the induced flow behind the incident shock wave, which has travelled through a turbulence-generating grid.

Figure 3 demonstrates the density contours of a typical experiment along the 12 in diameter shock tube with the 2 ft working section attached to it. All regions are clearly labelled, especially the useful data duration, which is of vital importance for uncontaminated data processing. In general, it is clear that the induced flow is separated into three distinct regions: passing through the grid; followed by the transient interaction with the expansion wave (non-stationary region); and after that, decaying in the region after the interaction. The latter is a region of interest. One of the controlling parameters for that interval is the initial bursting pressure in the driver section (P_4). The TVD program was used to simulate different ranges of pressure to optimize for the one that gives the longest flat region after the expansion has passed.

The working (test) section is fitted with several hot-wire and pressure ports. Thus, pressure, velocity and temperature data can be acquired simultaneously at various locations downstream of the grid, and therefore reduce the variance between measurements. High-frequency response pressure transducers and hot-wire anemometry have been used in the present investigation. Pressure transducers were placed throughout the driven section in order to monitor the passage of the shock wave and also to check its uniformity through the driven section. For the present experiments of velocity and vorticity measurements, high-frequency response Kulite pressure transducers (type XCQ-062) were installed in the shock tube at several locations, so that wall pressure could be measured simultaneously as a function of time.

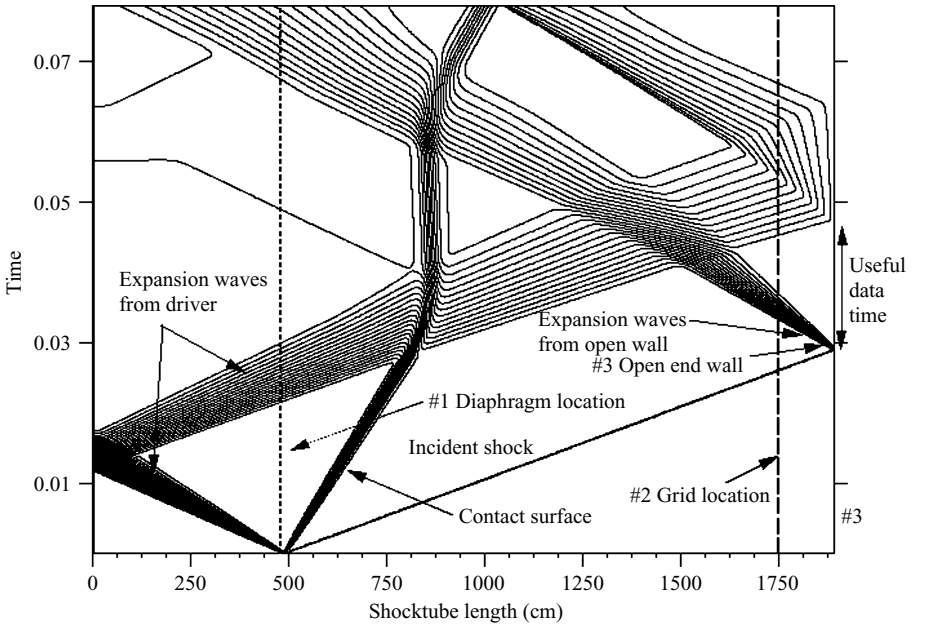

FIGURE 3. Density contours along the length of shock tube. $P_4 = 217.2$ kPa.

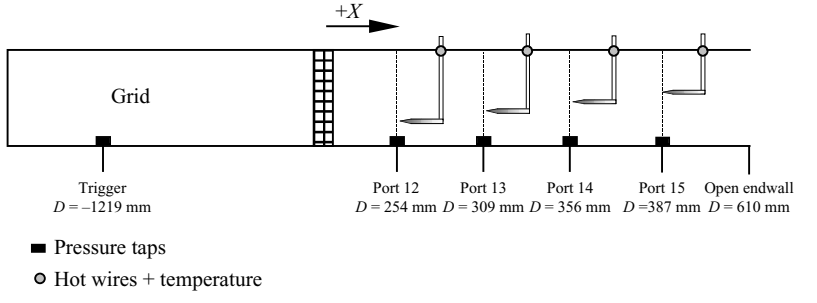

FIGURE 4. Two-dimensional schematic of the working section with pressure and hot-wire tap locations along the 2 ft length for the experiments with X-wires. (Not to scale).

To resolve simultaneously two-dimensional velocity components with hot wires, a cross-wire (X-wire) arrangement was used. New three-wire probes were designed and custom built. Five different three-wire probe assemblies were used concurrently at different downstream locations, all adjustable to different lengths, each carrying two hot wires in an X configuration and one cold wire for simultaneous velocity and temperature measurements, respectively. The three-wire probes were equipped with 5 μm platinum/tungsten wires for velocity measurements and with a 2.5 μm platinum/tungsten wire for temperature measurements. This experimental set-up (figure 4) provided time-dependent measurements of two-velocity components, temperature and wall pressure at several locations of the flow field simultaneously.

The cross-wires were driven by DANTEC anemometers (model CTA56C01) and the temperature wires were connected to EG&G model 113 low-noise battery-operated pre-amplifiers/filters. The output signal of the cold wire was digitally compensated for thermal lag up to frequencies of interest. For more details on the hot-wire techniques

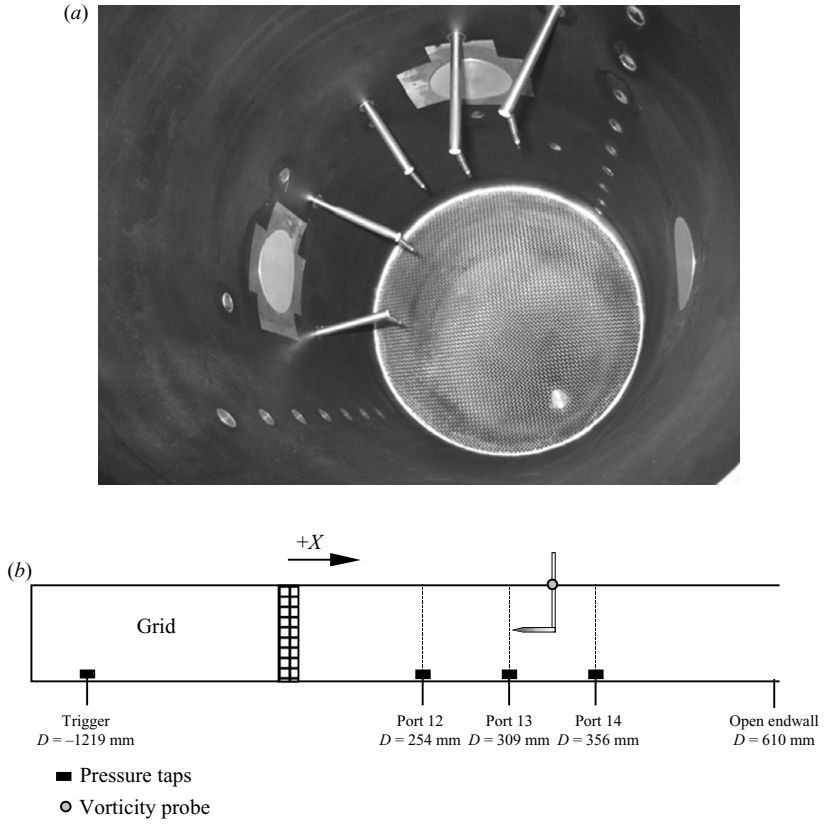

FIGURE 5. (*a*) Cross-wire probes staggered along the working section. (*b*) Two-dimensional schematic of the working section with pressure and vorticity probe locations along the 2 ft length. (Not to scale.)

applicable to shock tubes, see Briassulis *et al.* (1995) where estimates of uncertainties in the measurements are also given.

To eliminate any wake effects from probes located upstream, all the probes were staggered at increasing distances from the tube wall with downstream station and at different azimuthal positions (see figure 5*a*).

In addition, time-dependent three-dimensional vorticity measurements were carried out by using a new vorticity probe (see Agui 1998; hereinafter referred to as ABA; Andreopoulos & Honkan 1995; Honkan & Andreopoulos 1997*a*; Briassulis, Agui & Andreopoulos 2001). Figure 5(*b*) shows the arrangement for the simultaneous measurements of vorticity and wall pressure.

The shock tube was pressurized so any leaks could be detected, as well as to calibrate the pressure transducers. The shock tube was free of leaks and the static response of the transducers was found to be linear. Aluminium plates were used as diaphragms and were placed between the driver and the driven, initially conically shaped, section.

A detailed description of the facility and the results of the qualification tests can be found in Briassulis *et al.* (1995) and BAA. Details of this set-up can be found in Agui, Briassulis & Andreopoulos (2005), hereinafter referred to as ABA.

All data were digitized by four National Instruments analogue-to digital-converters (model NI PCI 6120) with 16 bit resolution and 800 kHz per channel for a total of

16 channels. The data acquisition system was triggered by the arrival of the shock wave at the location of a wall pressure transducer upstream of the grid. The grid was installed in the beginning of the working section.

The frequency response of the hot-wire probes, as measured during the passage of the incoming shock wave which provided the input step change, was found to be of the order of 100 kHz. This value is based on the spatially averaged longitudinal velocity at the centroid of the probe. The cold-wire signal had a flat frequency response up to about 8 kHz and it has been digitally compensated (see Briassulis *et al.* 1995).

Tables 1 to 4 provide information on the bulk parameters and operating conditions of the experiments.

3. Vorticity measurements

The vorticity probe developed and used in our previous work (BAA; ABA) has been also used in the present investigation. The probe is capable of measuring velocity-gradient related quantities in non-isothermal flows or in compressible flows. The present design is the outcome of our experience gained with vorticity measurements in incompressible flows by using a probe with nine wires, and with velocity measurements in compressible flows by using single- and cross-wire probes (sees Briassulis *et al.* 1995; ABA).

The present vorticity probe consists of 12 wires arranged in three modules (figure 6). Each module contains four sensors; three hot-wire sensors operated in the constant temperature mode (CTM) and one cold-wire sensor operated in the constant current mode (CCM). The three wires on each module are mutually orthogonal to each other oriented at 54.7° to the probe axis. Each of the 5 μm diameter tungsten hot-wire sensors was welded onto two individual prongs, which have been tapered at the tips. Each sensor is operated independently since no common prongs are used. Each of the 2.5 μm diameter cold wires was located on the outer part of the submodule.

Extensive testing of the probe has been carried out to assess its performance in shock-tube flows. See BAA and ABA for details of the tests and the techniques associated with the use of the probe. The probe was also tested in low-speed incompressible boundary-layer flows where vorticity measurements have been obtained in the past with a nine-wire probe and with optical techniques (see Agui & Andreopoulos 2003). The data obtained with the new probe compared well with these previous measurements.

The data processing started with the cold-wire signals which were first converted to total temperature. This information was used subsequently to obtain instantaneous three-dimensional mass fluxes at three neighbouring locations within the probe. These mass fluxes and their gradients were computed at the centroid of each module and some corrections were applied which accounted for the mass flux gradients across each module by using numerical techniques and algorithms used in the computations of mass-flux gradients which were similar to those described by Honkan & Andreopoulos (1997*a*, *b*).

Density and velocity information was recovered from the mass fluxes by decoupling density from mass fluxes assuming that static pressure fluctuations are small (see Briassulis *et al.* 1995). This assumption represents the so-called 'weak' version of the original 'strong Reynolds analogy' hypothesis of Morkovin (1955) since total temperature fluctuations are not considered very small as in the original hypothesis. It should be noted that in the present work, total temperature was measured directly and therefore no corresponding assumptions were required. The assumption about pressure fluctuations is fully justified since the measured root mean square (r.m.s.) of pressure in the boundary

	Grid size (meshes/in)	Mesh size (mm)	Solidity	p_2 (kPa)	U_{2u}	U_{2d}	T_{ou}	T_u	T_{od}	T_d	C_u Sound speed	C_d Sound speed	M_2	W_s (m s^{-1})	Re_M	ρ_u/ρ_d (kg m^{-3})
1	$2 \times 2a$	12.7	0.39	43.77	104	187	350	342	294	278	362	334	0.2528	405.00	122 000	1.55/1.25
2	$2 \times 2b$	12.7	0.28	46.18	106	190	345	339	290	272	366	330	0.2609	407.25	122 000	1.53/1.20
3	3×3	8.5	0.39	46.53	115	170	350	340	305	285	365	338	0.2629	407.75	82 000	1.55/1.21
4	4×4	6.35	0.44	41.02	94	175	342	335	293	280	361	335	0.2368	400.00	61 000	1.52/1.15

TABLE 1. Flow properties in experiments of vorticity measurements. Subscripts u and d indicate upstream and downstream conditions, respectively.

	Grid size (meshes/in)	p_2 (kPa)	U_{2u}	U_{2d}	T_{ou}	T_u	T_{od}	T_d	C_u Sound speed	C_d Sound speed	M_2	Re_M	ρ_u/ρ_d (kg m^{-3})
1	$2 \times 2a$	38.75	98	160	340	332	276	259	359	323	0.2609	110 000	1.45/1.29
2	$2 \times 2b$	42.5	99	178	330	321	270	251	358	319	0.277	110 000	1.48/1.26
3	3×3	28.61	85	150	320	316	290	278	356	334	0.239	52 000	1.43/1.22
4	4×4	40.68	112	190	335	328	282	263	364	326	0.30	68 000	1.50/1.29
5	8×8	42.6	120	185	330	323	282	270	361	329	0.33	35 000	1.51/1.25

TABLE 2. Flow properties in experiments with X-wires. Subscripts u and d indicate upstream and downstream conditions, respectively.

	Grid size (meshes/in)	S_{11} (s^{-1})	$1/S_{11}$ (ms)	$S_{11}L_\varepsilon/q$	L_ε/q (ms)	q ($m\,s^{-1}$)	ε ($m^3\,s^{-2}$)	Re_λ	M_g $L_\varepsilon S_{11}/C_u$	M_t q/C_u
1	$2\times 2a$	218	4.58	14.32	65.7	4.97	376	488	0.226	0.0137
2	$2\times 2b$	161	6.21	8.405	52.2	5.22	419	426	0.105	0.0142
3	3×3	250	4.00	4.780	19.00	5.27	1462	450	0.070	0.0144
4	4×4	176	5.68	6.140	34.89	3.28	309	344	0.055	0.0090
5	8×8	190	5.20	2.488	12.94	5.10	2120	310	0.034	0.0140

TABLE 3. Incoming flow bulk parameters.

	Grid size (meshes/in)	Mesh size (mm)	L_ε (m)	λ (mm)	η (mm)	L_{11} (m)	L_{11}/L_ε
1	$2\times 2a$	12.7	0.376	1.96	0.058	0.0340	0.0920
2	$2\times 2b$	12.7	0.24	1.61	0.056	0.0295	0.1220
3	3×3	8.5	0.101	1.79	0.041	0.0320	0.3160
4	4×4	6.35	0.114	2.07	0.060	0.0415	0.4080
5	8×8	3.17	0.066	1.20	0.036	0.0200	0.3030

TABLE 4. Length scales of incoming flow.

layer is below 1 % of the mean wall pressure. In addition, the measured mean pressure gradient in the radial direction was found to be negligible. This allowed the mean value of the wall pressure signal to be extrapolated to the location of the hot-wire probes and to be used to separate the density and velocity signals since no mean pressure variation has been detected across a given section of the flow. The computational procedure involves an expression for mass flux, m_i, in terms of total temperature, T_0, and pressure, p, at the centroid of each array $m_i = \rho U_i = pU_i/RT = pU_i/[R(T_0 - U_k U_k/2c_p)]$, where U_i is the instantaneous velocity component, $i = 1$, 2 or 3 and $U_k U_k = U_1^2 + U_2^2 + U_3^2$. By using Reynolds decomposition, the velocity was further decomposed into its mean and fluctuating parts as $U_i = \bar{U}_i + u_i$. Full decoupling of density and velocity was achieved through an iterative scheme. In the first iteration, the effect of the lateral velocity components in the spanwise and normal directions, was assumed to be substantially smaller that the quantity $T_0 - U_1^2/2c_p$. Then, the above relation can be rearranged to obtain a quadratic equation for U_i, $(Rm_i/2c_p)U_i^2 + pU_i - m_i RT_0 = 0$ which has always one root positive and one negative. The positive root only was accepted since the negative root is unrealistic. The longitudinal velocity component U_1 was computed first whereas the other two components were obtained from the mass flux ratios as $u_2 = m_2/m_1 U_1$ and $u_3 = m_3/m_1 U_1$. The values U_1, U_2 and U_3 provided the first estimate of the velocity components and were used subsequently to obtain a better estimate of the $U_k^2/2c_p$. This iterative scheme required no more than two iterations for convergence.

The streamwise derivatives of the three velocity components usually require the use of Taylor's hypothesis of 'frozen' convected turbulence to convert temporal derivatives of velocity into spatial derivatives. In the present work, this has been accomplished by considering the use of the full momentum equations to estimate the streamwise derivatives of the three velocity components by ignoring the viscous terms. These expressions can be written as

$$\frac{\partial U_1}{\partial x_1} = -\frac{1}{U_1}\left[\frac{\partial U_1}{\partial t} + U_2\frac{\partial U_1}{\partial x_2} + U_3\frac{\partial U_1}{\partial x_3} - \frac{1}{\rho}\frac{\partial p}{\partial x_1}\right], \tag{3.1a}$$

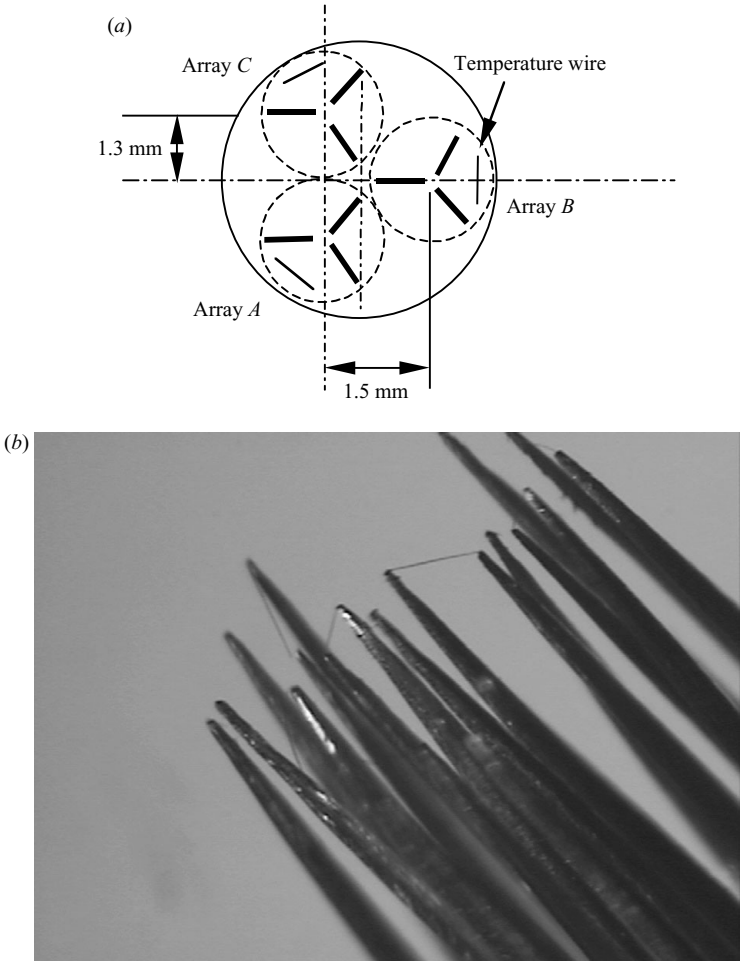

FIGURE 6. Vorticity probe: (*a*) probe sensor geometry and arrays, (*b*) close-up view of the probe.

$$\frac{\partial U_2}{\partial x_1} = -\frac{1}{U_1}\left[\frac{\partial U_2}{\partial t} + U_2\frac{\partial U_2}{\partial x_2} + U_3\frac{\partial U_2}{\partial x_3} - \frac{1}{\rho}\frac{\partial p}{\partial x_2}\right], \tag{3.1b}$$

$$\frac{\partial U_3}{\partial x_1} = -\frac{1}{U_1}\left[\frac{\partial U_3}{\partial t} + U_2\frac{\partial U_3}{\partial x_2} + U_3\frac{\partial U_3}{\partial x_3} - \frac{1}{\rho}\frac{\partial p}{\partial x_3}\right]. \tag{3.1c}$$

Thus, the determination of the streamwise gradients $\partial U_i/\partial x_1$ is not based entirely on the original Taylor's hypothesis. All the terms in the above are available at each time step, with the exceptions of the pressure gradients. Mean values of pressure gradients in the lateral directions are zero and their fluctuations are extremely small. In that respect, $\partial p/\partial x_2$ and $\partial p/\partial x_3$ have been neglected in the corresponding equations. The pressure gradient, $\partial p/\partial x_1$, which appears in the streamwise gradient of the longitudinal velocity is not zero through the flow expansion zone. Figure 7(*a*) shows three wall pressure signals obtained at three different locations below the hot-wire probes in the working section. Their temporal gradients, $\partial p/\partial t$, are also shown in the same figure. These temporal gradients were converted to spatial gradients of pressure, $\partial p/\partial x_1$, by considering their propagation into the upstream flow which

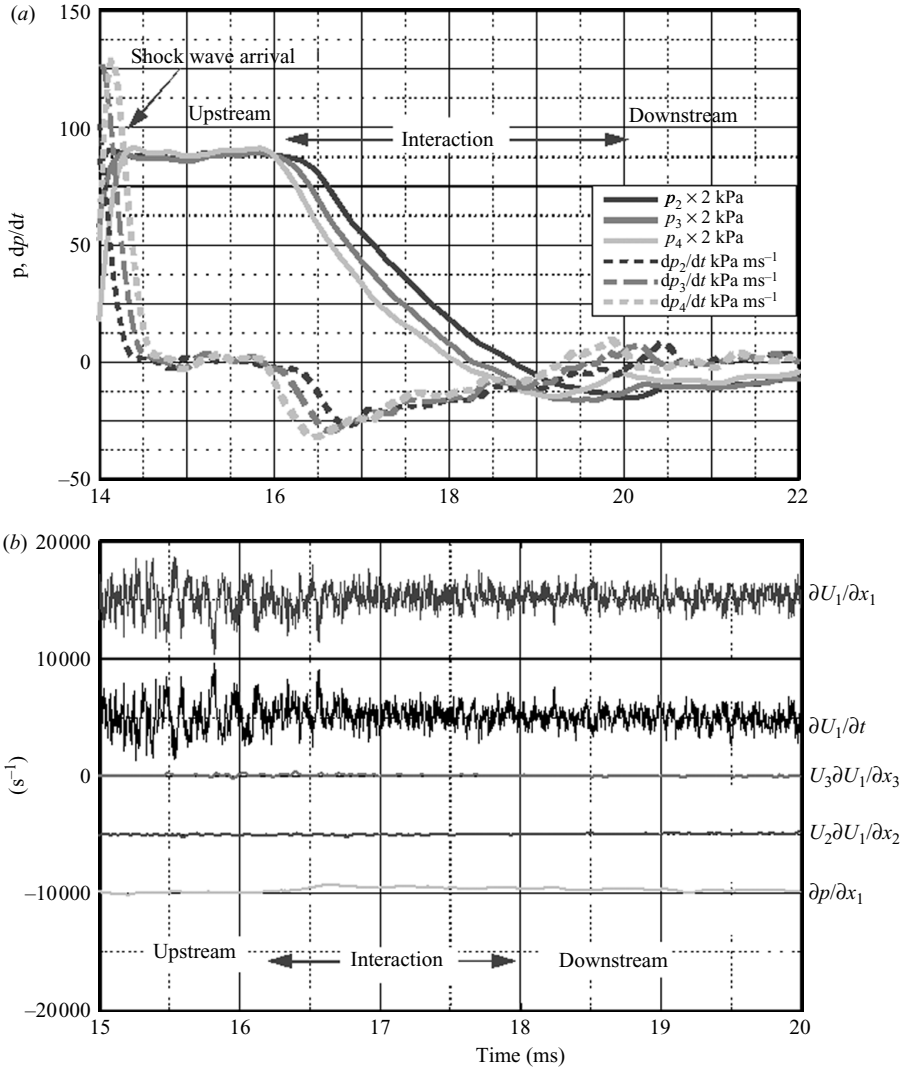

FIGURE 7. (*a*) Typical time-dependent wall pressure signals and their temporal gradients at three different locations in the working section below hot-wire probes for a $2 \times 2a$ grid. (*b*) Computation of velocity gradient, $\partial U_1/\partial x_1$, from contributing terms, case of 4×4 grid. Signals are shifted by multiples of 5000 s^{-1}.

takes place with a relative velocity equal to that of the local speed of sound, C. This propagation velocity of EW relative to laboratory coordinates is $C(t) - U_1(t)$ where U_1 is the local flow velocity. Both time-dependent quantities, C and U_1, are available from the combined temperature and velocity measurements. In that respect, the spatial gradient was evaluated from the temporal gradient through the relation $\partial p/\partial x_1 = -(\partial p/\partial t)(1/(C - U_1))$. The contribution of this term as well as those of the other terms into the final computed value of $S_{11} = \partial U_1/\partial x_1$ is demonstrated in figure 7(*b*) where each of the individual terms is plotted separately.

The data in figure 7(*b*) clearly show that the major contribution to S_{11} comes from the term $-1/U_1 \partial U_1/\partial t$ which provides most of its high-frequency content. The terms $-U_2/U_1 \partial U_1/\partial x_2$ and $-U_3/U_1 \partial U_1/\partial x_3$ are substantially smaller than the

leading term, a finding which also agrees with BAA and ABA. The contribution from the pressure gradient term $1/(\rho U_1)\partial p/\partial x_1 = -1/(\rho U_1)\partial p/\partial t_1/(C - U_1)$ appears to provide a low-frequency content of modest amplitude in the final value of $\partial U_1/\partial x_1$. The only assumption made in the present analysis is that the magnitude of the pressure fluctuations inside the flow field is negligible to the mean pressure upstream and downstream of the interaction or to the slowly varying pressure within the expansion zone. This assumption introduced an uncertainty into the computations which will be considered below. It should be emphasized that only S_{11} is affected directly by the pressure gradient along the straining expansion zone where the interaction takes place. The rest of the velocity gradients and therefore all components of vorticity, are not affected directly by pressure gradients.

4. Probe interference with expansion waves

The present flow is configured in a shock tube by taking advantage of the induced flow behind a moving shock wave and using hot-wire probes to measure velocity which although small in size can, in principle, interfere with the flow. The incident shock wave impinges on the probe and its holder, reflects, and wraps around the probe. It regroups quickly after this into a planar shock, again moving towards the open endwall of the shock tube where it reflects as a set of expansion waves travelling in the opposite direction. Although the hot-wire sensors are always measuring velocity vectors with a predominant orientation in the downstream direction, the expansion waves travel in the opposite direction, they may interact with the probe holder and the after-body of the hot-wire probe and alter the measured velocity field indirectly. In order to estimate the aerodynamic interference effects between the multi-wire probe and the moving expansion waves, a computational fluid dynamics study has been undertaken by fully simulating the time-dependent three-dimensional flow field around the probe under the same conditions as those in the shock-tube flow. A wire frame model of the actual probe was created in GAMBIT (figure 8*a*, *b*) and meshed so that the flow field at the locations of the hot-wire sensors can be computed. An unstructured mesh with 560 000 cells was created and the time-dependent three-dimensional Reynolds-averaged Navier–Stokes equations were used. A second-order solver provided by FLUENT was used to compute the flow field. The line-averaged velocity vector along the cylindrical wire sensor was estimated at three different locations of these sensors and compared with the undisturbed free-stream velocity at a location above the probe at the same longitudinal distance. Results of the present three-dimensional viscous calculations are shown in figure 8(*c*, *d*) where pressure and velocity contours of the flow field around the probe are plotted immediately after the passage of the incident shock. The pressure and velocity contours show reflections of the shock wave over step changes in cross-sectional areas of the holder, but the flow field at the sensor areas is reasonably uniform after the shock-wave passage. Figure 8(*e*) shows the velocity contours during the passage of the expansion waves over the probe. No non-uniformities of the flow field at the sensor areas can be depicted. A more quantitative comparison of computed longitudinal velocity components at the wire locations with the undisturbed free-stream velocity can be seen in figure 8(*f*). The results indicate that the velocity at the wire locations closely follows the undisturbed velocity at all times of the flow field duration, even shortly after the passage of the incident shock wave. The velocity at the sensors increases during the passage of the expansion zone at the same rate as the free-stream velocity. The small variations of the velocity at all locations under consideration observed after

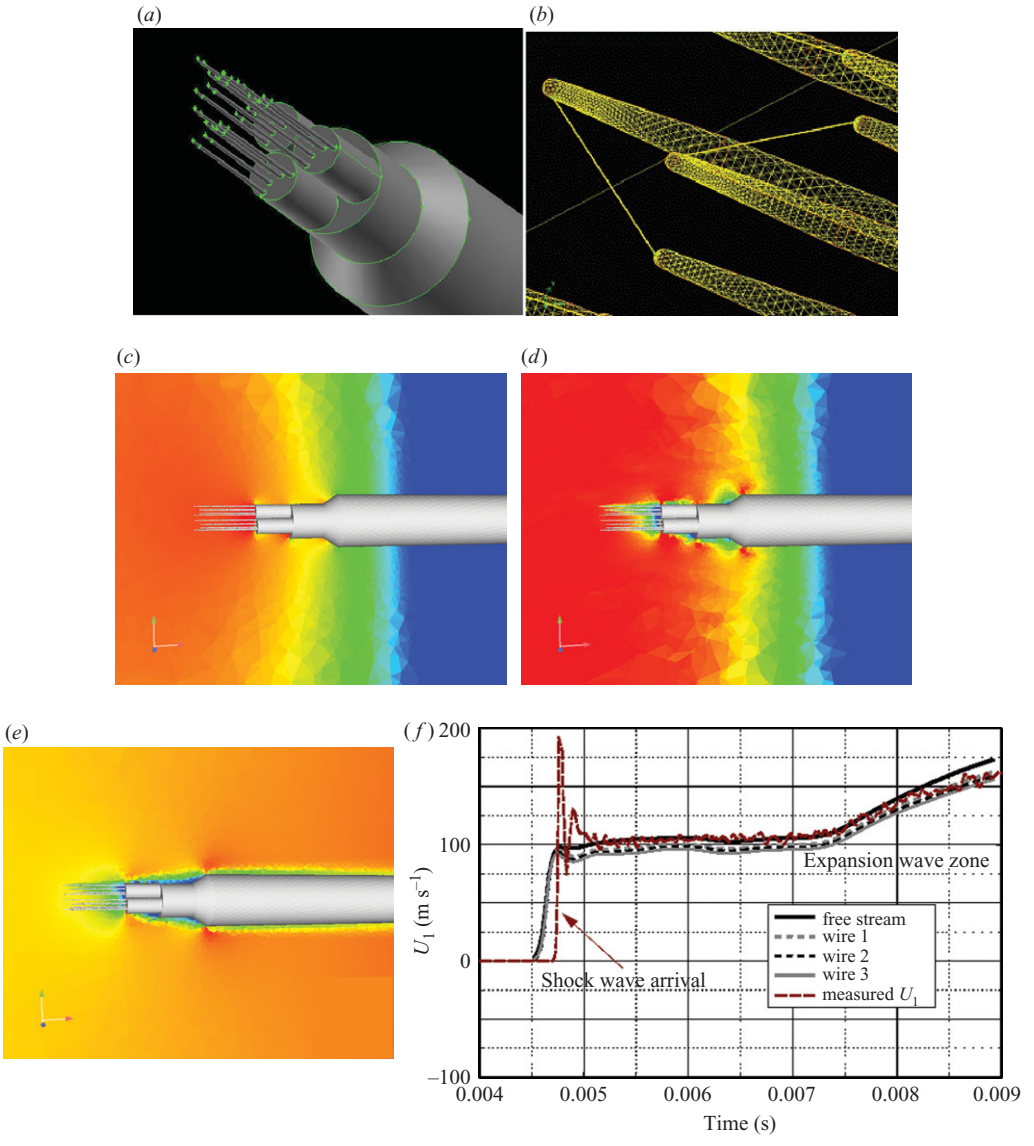

FIGURE 8. Vorticity probe model. (*a*) Wire frame; (*b*) close-up view of prongs area. Computed flow field after the passage of the incident shock, (*c*) pressure field (scale: red 5.617×10^4 to blue 2.519×10^4), (*d*) velocity field (scale: red 98.40 to blue 41.77). (*e*) Velocity contours during the passage of expansion waves (scale: red 1.973×10^4 to blue 3.760×10). (*f*) Computed longitudinal velocity component at locations of hot wires and free stream.

the passage of the shock are mostly due to the limited mesh size rather than to any physical cause. The computed values of the velocity also agree reasonably well with the measured values of the corresponding velocity component. This work indicates that there is no interference between the probe and the expansion waves and that the minor but consistent difference between measured and computed velocity magnitudes can be absorbed in the calibration coefficients of the probes.

5. Uncertainty estimates

The pressure and total temperature measurements depend directly, through obtained calibration constants, on the raw voltage data from the individual sensors. These probes, because of their linear response, produced two calibration constants, sensitivity and d.c. offset. Therefore, estimates of the uncertainty in the measurements of pressure and total temperature acquired through a 16-bit A/D converter depended mostly on the bit resolution and the residual errors from the calibration constants. Uncertainties of less than 0.5 % in pressure and about 2 % in total temperature were found for typical measurements of these two quantities.

The mass flux measurements were tied to significantly more complex relations, which depended on the individual and relative geometry of different sensors. Mass flux was found to depend on the following variables: captured raw voltage E_i, reference temperature T_r, total temperature T_0, wire temperature T_w, calibration constants and yaw or pitch coefficients. Uncertainty values for the velocity were estimated to be between 1 and 3 %. These values are slightly better than those in BAA and ABA because of higher resolution of the ADCs. In obtaining all these estimates, the square root of the squares of all partial uncertainties involved was assumed to model the error propagation into the final results. MATHCAD was used to calculate the partial uncertainties.

The density variation across the sensing area has been also estimated from the $\Delta p/p$ obtained above and the measured variation of total temperature T_0 through the uncertainty propagation formula

$$\frac{\Delta\rho}{\rho_0} = \left\{ \left[\frac{\Delta p}{p_T}\right]^2 + \left[\frac{\Delta T}{T_0}\right] \right\}^{1/2}.$$

This predicted approximately the same uncertainty as in the case of pressure variation.

Following ABA, estimates of the uncertainties associated with the measurements of velocity gradients were also obtained by considering the propagation of the uncertainties in the measurement of each quantity involved in the process. A typical velocity gradient is measured through the following approximation: $\partial U_i/\partial x_j \approx (U_2 - U_1)/l_p = F$ where U_2 and U_1 are the velocities at two nearby locations, l_p is the distance between these locations. If the uncertainties in the measurements of U_2 and U_1 are the same $\Delta U_1 = \Delta U_2 = \Delta U_3$, and l_p is determined accurately, then the relative uncertainty $\Delta F/F$ will be given by: $\Delta F/F = \{2[\Delta U/(U_2 - U_1)]^2\}^{1/2}$.

A typical ΔU is 2 % of mean U, which corresponds to about $2\,\mathrm{m\,s^{-1}}$ while typical velocity differences $U_2 - U_1$ can be up to six times the r.m.s. value, u'. If a typical value of this velocity difference is assumed of about $30\,\mathrm{m\,s^{-1}}$ in the near field of the grid and $15\,\mathrm{m\,s^{-1}}$ further downstream, then the uncertainty $\Delta F/F$ appears to be 10 % in the near field and 14 % in the far field.

It has been shown in ABA that in the limit of infinite resolution, i.e. for $\Delta x_j \to 0$, that

$$\overline{\left(\frac{\Delta U_i}{\Delta x_j}\right)^2}_{\Delta x_j \to 0} = \frac{\overline{[U_i^2(x_j)]}}{\lambda_{ij}^2}$$

where λ_{ij} is the corresponding Taylor's microscale, which suggests that the velocity gradients scale with λ_{ij}. If this relation is used as $\partial U_i/\partial x_j \approx u'/\lambda = F$, then lower uncertainty estimates have been found. In this case, the relative error is $\Delta F/F = \{(\Delta u'/u')^2 + (\Delta\lambda/\lambda)^2\}^{1/2}$. For a typical relative error in u' of 5 % and 10 % in λ, the relative error appears to be about 11 %. It should be noted that the relative error

$\Delta F/F$ increases as the distance from the grid increases because the absolute value of F decreases.

Finally, the finite number of statistically independent events considered in the data analysis of certain flow cases introduces an uncertainty in the statistical results. Computations of the integral time scale, L_t from auto-correlation functions $R_{11}(\tau)$ indicated that the number of independent samples, in general, was between 80 to 120. Downstream of the interaction, L_t decreases and the number of statistically independent events is increased.

The onset of the useful data duration in the upstream of the interaction region is also delayed by the arrival of the air mass, which has not passed through the grid. The number of independent samples in these cases was about $N \approx 60$–100. Bendat & Piersol (2000) indicate that the relative error in the estimate of the variance of the velocity fluctuations is $2/N$, which for this specific case is between 2 to 4 %. It should be noted that N depends on the shape of R_{11} that can be extended to large values if low-frequency variations are present in the flow-field. In the case of high-pass filtered data, which are discussed in the next section, L_t is reduced substantially and N increases by a factor of 2.

More direct evidence of the adequacy of statistical samples can be provided by the rate of convergence of the various statistical quantities, which are computed in the present data analysis. As shown in BAA, estimates of the convergence uncertainties observed in the present analysis indicate an error of less than 3%. This error is substantially less at higher Mach numbers and closer to the grid locations.

It should also be mentioned that the above discussion is mostly pertinent to the statistics of velocity components. Most of the contributions to vorticity and velocity gradient statistics come from events of much smaller size than those represented by the integral time scales. These are plentiful and therefore there is no effect on their statistics because of finite number of statistically independent events.

The spatial resolution of the probe is between 0.6λ and 1λ upstream of the shock region and between 0.4λ and 0.6λ in the downstream region. The scales of error expressed in Kolmogorov's viscous scale $\eta = (\nu^{3/4}/\varepsilon)^{1/4}$ appear to be in the range of 8η–15η upstream of the interaction region and improve substantially downstream of the interaction because the length scales increase. In that respect, the expected attenuation of the measurement of vorticity r.m.s. owing to limited spatial resolution is not significant.

6. Data analysis, decomposition and reconstruction

A closer look into the time-dependent signals within the EW indicated that several quantities are characterized by a low-frequency variation which starts at the head of the EW fan and ends at its tail, and a higher-frequency component which could be attributed to turbulence. In that respect, all time-dependent signals have been decomposed into two major components, one with low-frequency content and one with high-frequency contributions by low-pass and high-pass filtering the signals. Thus, a typical quantity $Q(t)$ is decomposed as

$$Q(t) = Q_{LP}(t) + Q_{HP}(t). \tag{6.1}$$

This decomposition can be considered as a direct outcome of the Fourier series expansion in-time of the original signal and separating the two components below and above a certain frequency. In practice, however, low-pass and high-pass filtering of the original signals causes some distortion around the cut-off frequency, which

is the same for both filtering operations. The time scales of the expansion wave passage and the time scales of turbulence were reasonably far apart from each other, and therefore no information has been compromised by the data filtering. Low-pass filtering removed the fluctuations due to turbulence from the signal so that the characteristics of the expansion zone were revealed since they were separated from turbulence. High-pass filtering removed the low-frequency effects of the expansion waves and only turbulent fluctuations were retained with zero mean. This operation is called trend removal in signal processing.

Figure 9(*a*) shows the decomposition of longitudinal velocity U_1 into its low- and high-pass filtered components, $U_{1,LP}$ and $U_{1,HP}$, respectively. The low-pass component represents the trend in the velocity increase owing to the flow acceleration caused by the passage of the EW and it is free of any frequency content above the 500 Hz cutoff value. The HP filtered component does not show low-frequency components or trend and it includes the high-frequency components of the signal. In order to demonstrate the effectiveness of the decomposition, the two components have been re-combined to form the reconstructed signal $Q_{LP}(t) + Q_{HP}(t) = Q_R(t)$, which does not differ from the original signal $Q(t)$ (see figure 8*a*).

All the components of the velocity gradient tensor exhibit practically a zero mean value within the EW with the exception of S_{11} which shows a trend, i.e. a low-frequency component which shows some variation with time. The decomposition of S_{11} into LP and HP components is shown in figure 9(*b*). It appears that the reconstructed signal is identical to the original one, indicating that the decomposition does not distort the signal. It also suggests the validity of this process. The LP component increases slightly directly after the encounter with the head of the EW and it shows a positive value within the interaction zone which is slowly decreasing towards the tail of the EW.

The LP component of the vorticity component Ω_3 (figure 9*c*) does not show any low-frequency content of appreciable amplitude. As a result of this decomposition, the HP components of all quantities represent the true turbulence, uncontaminated by the effects of a low-frequency trend and therefore they can be further processed to identify the effects of EW on turbulence. All HP signals now have a zero mean value and they are non-stationary. In order to demonstrate the amplitude of the fluctuations within this interaction, the region was subdivided into several subregions of shorter time than the EW time scale and the r.m.s. of the fluctuations within each of these subregions was computed. This short-time averaged information within each of the zones is not an accurate value of the true r.m.s. because the process is not stationary. It represents, however, a reasonably good estimate of the amplitude of the fluctuations within each subregion. In some respects, the processes involved can be considered as quasi-stationary within each of these subdivisions. These r.m.s. values, $\langle \sigma_i \rangle$, are normalized by the corresponding r.m.s. value in the upstream region, σ_u, which has been calculated from the data in the quasi-steady part of the signal upstream of the EW. The r.m.s. value in the region downstream of the EW, σ_d, has been similarly calculated from the quasi-steady data after the interaction. Both σ_u and σ_d represent the true values of the corresponding quantities which have been tested for convergence and stationarity in the regions before and after the passage of the EW. Thus, the ratio $\langle \sigma_i \rangle / \sigma_u$ indicates amplification or attenuation of the fluctuations within the interaction.

This data analysis was conceived to demonstrate the decay of fluctuations of several quantities within the EW which appears to dampen their amplitude. The data of $S_{11,HP}$, for instance (figure 9*b*), clearly demonstrate a pattern of decaying fluctuations within the EW. Figure 10(*a*) shows the variation of these short-time averages, $\langle \sigma_i \rangle / \sigma_u$ within

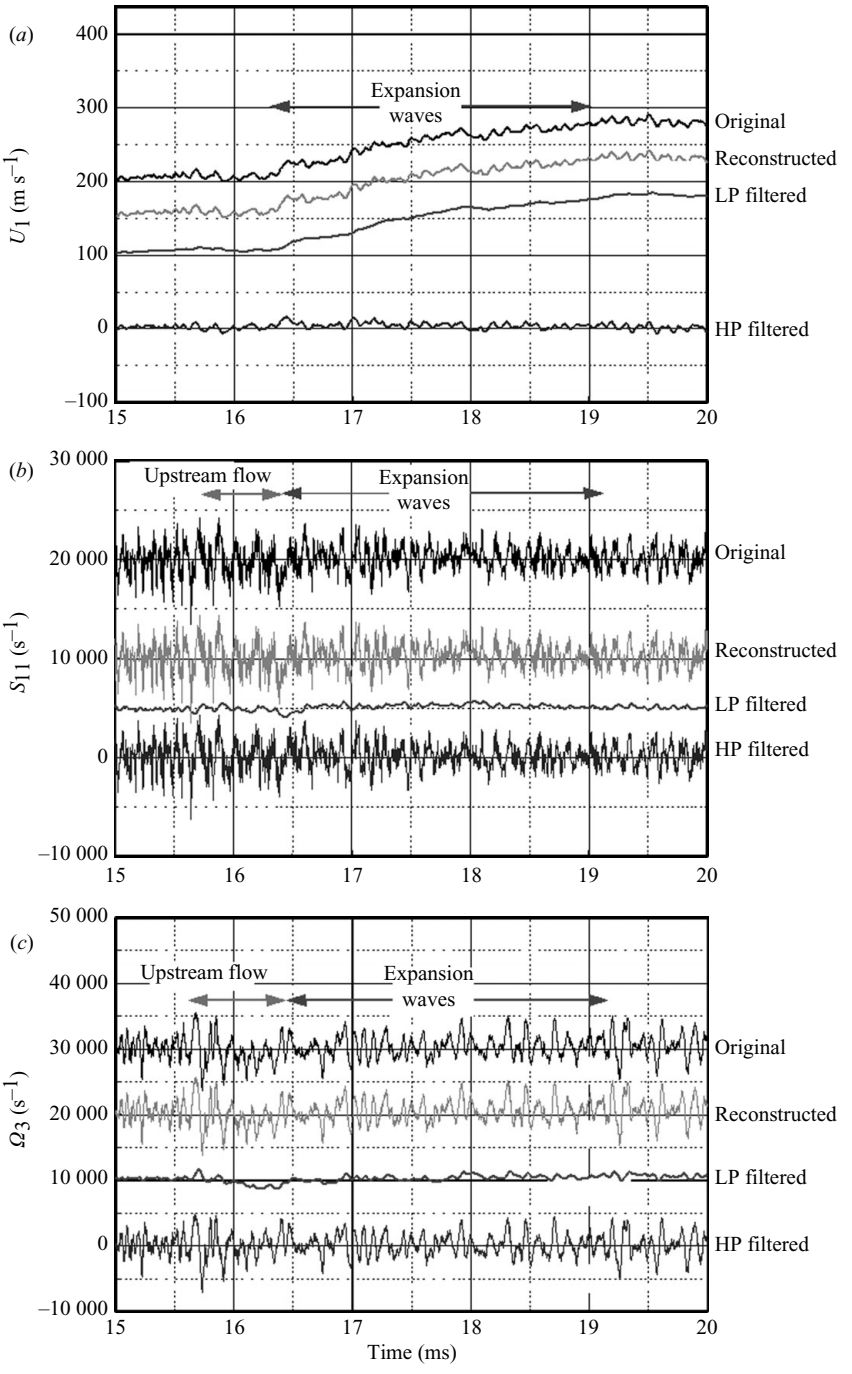

FIGURE 9. (*a*) Decomposition of U_1 signal into low- and high-pass filtered contributions. Original and reconstructed signals are shifted by $50\,\mathrm{m\,s^{-1}}$ and $100\,\mathrm{m\,s^{-1}}$ respectively. (*b*) Decomposition of S_{11} signal into low- and high-pass filtered contributions. Signals are shifted by multiples of $5000\,\mathrm{s^{-1}}$. (*c*) Decomposition of Ω_3 signal into low- and high-pass filtered contributions. Signals are shifted by multiples of $10\,000\,\mathrm{s^{-1}}$.

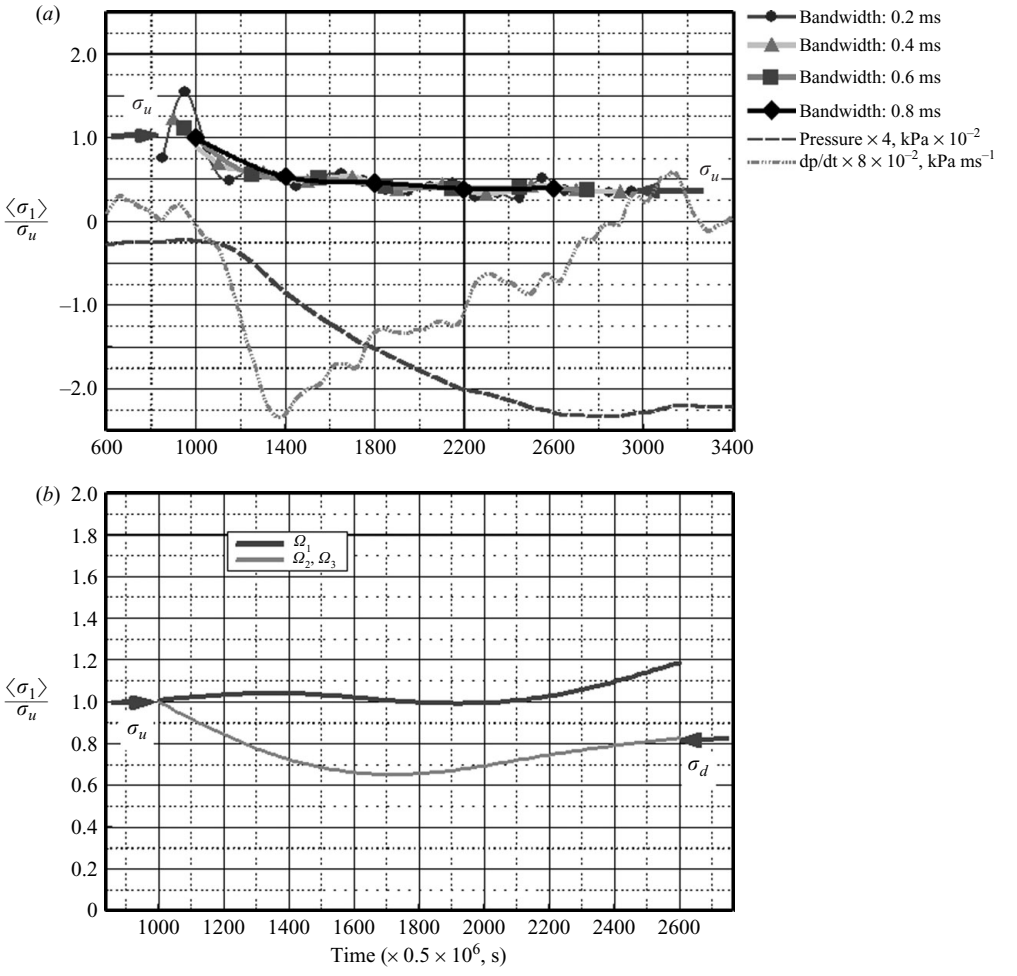

FIGURE 10. (*a*) Short-time averages of S_{11} r.m.s. fluctuations within the interaction zone of expansion waves (3 × 3 grid). (*b*) Short-time averages of r.m.s. of vorticity fluctuations within the interaction zone of expansion waves.

the EW for different durations, i.e. bandwidths of each of the subregions. In the case of the shortest bandwidth of 0.2 ms, the EW zone was subdivided into 20 subregions, whereas in the case of the largest bandwidth of 0.8 ms, the EW was subdivided into 5 subregions. The length of these subdivisions affects the first 50 % of the EW only, whereas the second half is practically independent of the length/bandwidth of the subdivisions, and the values of $\langle \sigma_i \rangle$ in the first half of the EW decrease with increasing bandwidth.

A closer look at these results indicates that the pressure gradient peaks very close to the beginning of the interaction region, i.e. within the first 15 % of its total duration, which roughly corresponds to the location of the maximum reduction rate in $\langle \sigma_i \rangle / \sigma_u$. Then it starts to relax some of its strength and reaches values close to zero at the end of the duration of the interaction. In the second half of the interaction where $\partial p/\partial t$ reaches values closer to zero, the level of amplitude fluctuations of S_{11} appears to be relatively independent of time and to be close to the downstream value, σ_d which is smaller than the upstream value of σ_u suggesting a substantial attenuation

of S_{11} fluctuations that is more than 50 %. It should be noted, however, that S_{11} is the quantity which is affected the most by the interaction with the EW. It is also the only quantity which is affected the most by the length/bandwidth of the subdivisions in the first half of the interactions. The remaining quantities considered here are much less influenced by the choice of the bandwidth.

The distribution of the short-time r.m.s. values of fluctuations of the three vorticity components is shown in figure 10(*b*). The amplitude of fluctuations of the lateral vorticity components appears to be changing in the first half of the interaction. In the second half, the amplitudes of Ω_2 and Ω_3 fluctuations appear to have been stabilized towards the r.m.s. value of the downstream of the interaction region, while the amplitude of the Ω_1 fluctuations still wanders around. At the end of the interaction, the true r.m.s. of the fluctuations of the two lateral vorticity components has been substantially reduced by about 20 % through the interaction while the longitudinal vorticity r.m.s. has been slightly amplified by 17 %. One critical observation in this behaviour is that although the incoming turbulent flow is reasonably isotropic, the outcome of the interaction is a rather strongly non-isotropic flow field. This behaviour, which is related to the return to isotropy, still has to be further investigated.

7. The flow field

There is a substantial amount of data documenting the homogeneity and uniformity of the upstream and downstream of the interaction flow region (see BAA; ABA). The present data also suggest that the flow within the interaction remains reasonably uniform in the radial and azimuthal directions, while acceleration takes place in the longitudinal direction. Evidence of this is shown in figure 11(*a*), where the time-dependent low-pass filtered pressure signals shown originally in figure 7(*a*), have been shifted in time by an amount equal to the flight time of the head of the expansion waves required to travel from one to the next pressure transducer location. The data indicate that the pressure and its temporal gradient remained unchanged in the longitudinal direction at fixed times, which implies that the pattern is convected without substantial deformation or distortion, although the tail of the EW is known to propagate with slightly slower speed than the head, and therefore the duration of the expansion waves increases slightly as they travel upstream.

Figure 11(*b*) shows the U_1 and U_2 velocity components obtained with cross-wire probes at two locations different in the longitudinal and radial directions. The two signals of the longitudinal velocity are close to each other in the upstream of the interaction region and they start to divert slightly from each other at the onset of the interaction. At the end of the interaction, the downstream hot-wire indicates velocities which are 2 to 3 % higher than those upstream. Although this difference is of the order of the uncertainty measurements, most probably, it can be attributed to viscous effects at the wall. The lateral components show no difference with downstream location change.

This small variation in the velocity components within the flow field suggests that the lateral strainings $S_{12,LP}$ and $S_{22,LP}$ are small. Additional wall-pressure data showed no circumferential variation. Thus, it is reasonable to conclude that the present homogeneous and isotropic flow is strained in the longitudinal direction only by the bulk straining $S_{11,LP}$. During the expansion of the flow, the lateral rate of strains $S_{12,LP}$, $S_{22,LP}$, $S_{13,LP}$ and $S_{33,LP}$ remain small and possibly unaffected by the reduction of the wall boundary-layer thickness owing to the sudden external flow acceleration. As a result of this bulk flow behaviour, the only key production term in

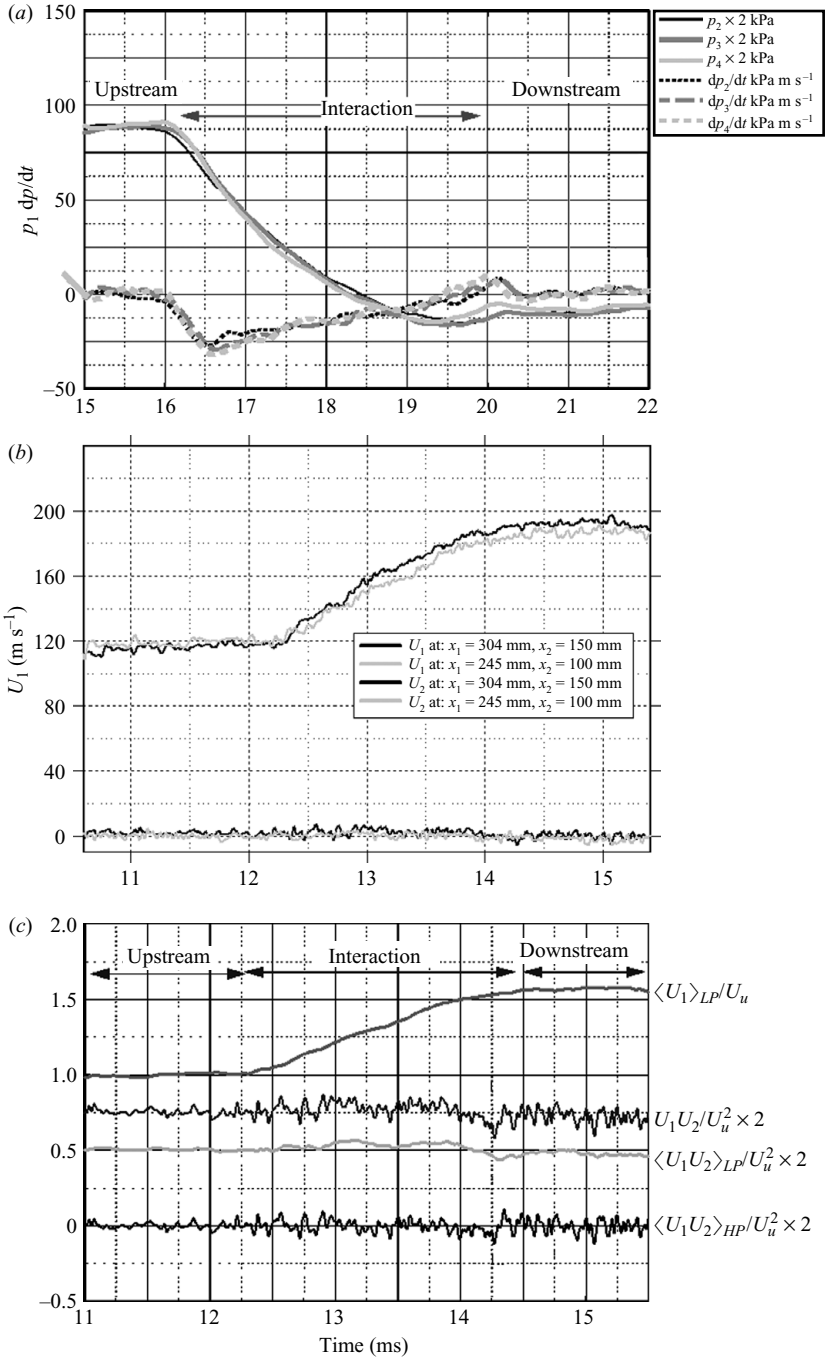

FIGURE 11. (*a*) Low-pass filtered pressure signals and their time derivative shifted in time within the expansion region. (*b*) Longitudinal and lateral velocity components at different locations obtained with X-wires for the case of the 8×8 grid. (*c*) $\langle U_1U_2 \rangle$ correlations before, during and after the interaction. The original U_1U_2 signal is twice amplified and displaced by 0.750 units. $\langle U_1U_2 \rangle_{LP}$ signal is twice amplified and displaced by 0.50 units. $\langle U_1U_2 \rangle_{HP}$ signal is twice amplified. All signals are normalized by the incoming velocity U_u.

the turbulent kinetic energy transport equation during the flow expansion appears to be the term $-u_1^2 S_{11}$. This term is always negative and since it acts as a sink, turbulence is suppressed during the interaction.

In the case of one-dimensional frictionless flow with left-running expansion waves moving relative to a flow with velocity equal to the speed of sound $C_u = (\gamma p_u/\rho_u)^{1/2}$, continuity of mass flow in a control volume fixed on the local expansion waves yields that the infinitesimal change of velocity across a short length of expansion waves after neglecting second-order differentials is

$$\mathrm{d}C = -C\frac{\mathrm{d}\rho}{\rho}, \tag{7.1}$$

with C being the velocity in the coordinate system associated with the head of the expansion waves. This can be integrated to obtain $\ln C = -\ln\rho + \ln A$ or $C\rho = A$ where A is a constant and therefore the relation between upstream (C_u, ρ_u) and downstream conditions (C_d, ρ_d) is $C_d/C_u = \rho_u/\rho_d$. The velocity difference $\Delta C = C_d - C_u = (\Delta\rho/\rho_d - 1)C_u$ is the velocity increase between the upstream and downstream regions in a reference coordinate system moving with the velocity C_u of the expansion waves and, in fact, it is the same in a laboratory coordinate system since the relative velocity of the moving expansion waves to the laboratory coordinates is $U_d - C_u$. Thus, $\Delta U = U_d - U_u = \Delta C$ is the same relative to laboratory coordinates.

After similar manipulations of the momentum equation, the following relation can be obtained for the pressure drop $\mathrm{d}p = -\rho C\mathrm{d}C$ which becomes

$$\mathrm{d}p = C^2\,\mathrm{d}\rho. \tag{7.2}$$

Integration between upstream and downstream conditions and use of continuity yields

$$p_d - p_u = C_u^2\rho_u^2\int_{\rho_u}^{\rho_d}\rho^{-2}\,\mathrm{d}\rho = -C_u^2\rho_u\left[\frac{\rho_u}{\rho_d} - 1\right].$$

For the measured data shown in figures 7(a) and 9(a), which are typical of the present experiments, with $p_u = 144\,\mathrm{kPa}$, and $\rho_d/\rho_u = 1.25/1.55$, the velocity and pressure changes predicted by these two equations appear to be $\Delta C = \Delta U = 0.24C_u = 86.4\,\mathrm{m\,s^{-1}}$. This is close to the measured $83.3\,\mathrm{m\,s^{-1}}$. For $C_u = 360\,\mathrm{m\,s^{-1}}$ we obtain $\Delta p = 48.2\,\mathrm{kPa}$, close to the measured 49 kPa. Thus, the measured mean quantities of velocity and pressure in the present experiments are reasonably close to those predicted by one-dimensional theory. In addition, the computed results of longitudinal velocity and pressure obtained in the CFD work related to the flow around the vorticity probe agree well with measured time-dependent quantities (see figure 8f).

The incoming flow is isotropic and therefore the time-average correlation U_1U_2 is expected to be small. Figure 11(c) shows signals of the time-dependent quantity U_1U_2 and its low- and high-pass filtered components $\langle U_1U_2\rangle_{LP}$ and $\langle U_1U_2\rangle_{HP}$, respectively. The low-pass filtered signal of the longitudinal velocity $\langle U_1\rangle_{LP}$ is also plotted for reference. The amplitude of the $\langle U_1U_2\rangle_{HP}$ component appears to be small in the upstream region and its mean value is close to zero. However, its fluctuations increase substantially during the interaction. This amplification starts from the beginning, immediately after the onset of the straining action and its amplitude is reduced slightly towards the end of the interaction and in the downstream region where time scales are faster than in the upstream region, and reaches a value which is much higher than in the upstream region.

The amplitude of the low-pass signal, which is displaced by 0.50 units, shows some small-amplitude variation, but its time-averaged value is close to zero before the

interaction. However, during the interaction, its amplitude increases substantially and large-scale variations appear which take some time to subside. Thus, the axisymmetric straining introduces a strong anisotropy into the initially isotropic field. The return to isotropy of the turbulent flow after the passage of the expansion waves is not that fast.

According to rapid distortion theory (RDT), in flows where turbulence is distorted by a rapidly applied mean shear $S_{11} = [\partial U_1/\partial x_1]_{Inter}$ that is produced by an expansion wave, the controlling parameter is the ratio of the timescale of turbulence $T_\varepsilon = L_\varepsilon/q$ to the time scale of the applied strain, $1/S_{11}$, i.e. $R_t = L_\varepsilon S_{11}/q$. L_ε is the dissipative length scale defined as $L_\varepsilon = q^3/\varepsilon$, q is the square root of the turbulence kinetic energy $q = [1/2\overline{u_i u_i}]^{1/2}$ and ε is the dissipation rate of turbulent kinetic energy q^2. Thus, the ratio appears to be $R_t = q^2 S_{11}/\varepsilon$. The full dissipation rate has been evaluated in the present work. In this case $E = E_s + E_d$ with

$$E_s = \mu \Omega_k \Omega_k + 2\mu \left[\frac{\partial U_i}{\partial x_j} \frac{\partial U_j}{\partial x_i} - S_{kk} S_{kk} \right], \qquad E_d = 4/3\mu/_{kk} S_{kk}.$$

The strain rate S_{11} is associated with the imposed disturbance. Mean values of S_{11} have been computed from the present data by averaging the time-dependent data over the duration of the distortion and the corresponding times scales T_{EW} are plotted in figure 12(a) as a function of the Reynolds number based on the Taylor's microscale λ together with the dissipative time scales L_ε and their ratio R_t. Values of T_{EW} appear to be fairly constant at most experiments, but at the two highest Re_λ they drop off because of slightly stronger interactions. The characteristic dissipative time scale of turbulence T_ε seems to increase with Re_λ. The ratio of the time scales R_t shows a trend to increase with Re_λ. However, its values are not all substantially greater than 1. These data indicate that the imposed disturbance is not as rapid in speed and duration as a shock wave, although faster than the corresponding eddy turn-over time T_ε, a feature which allows for analysis of data obtained inside the expansion wave. The evidence shown in figure 12(a) suggests that, for some cases, the use of RDT is marginally justified. A closer look of the time derivative of pressure shown in figure 11(a) indicates the existence of two time scales in this signal. The first one is associated with the onset of the interaction and the fast-changing rate towards its local extreme value, and the second one is associated with the relaxation process after the maximum effect has been applied. The latter time scale is about four times longer than the first one. If the time scale of the fast-changing part is used in R_t, its values will be higher by a factor of four, which provides a more comfortable range for the applicability of RTD.

The cumulative effects of flow straining can be expressed by the integral

$$A_s(t) = \int_{t_0}^{t} S_{11}(t')\,\mathrm{d}t'$$

which is now a dimensionless time variable. The lower limit of the integration is the starting point of the interaction, and the upper limit t is the current time. These integrated straining effects are shown in figure 12(b) plotted together with the corresponding wall pressure as a function of time. During the interaction, A_s increases with a fairly constant rate of $0.312\,\mathrm{m\,s^{-1}}$ and then downstream of the interaction reaches a reasonably constant value between 0.6 and 0.7. According to RDT, turbulence after the interaction depends only on the cumulative strain and not on the state of strain during the interaction. The roughly linear variation of A_s with time suggests that S_{11} can be approximated as constant during the interaction and therefore variations due

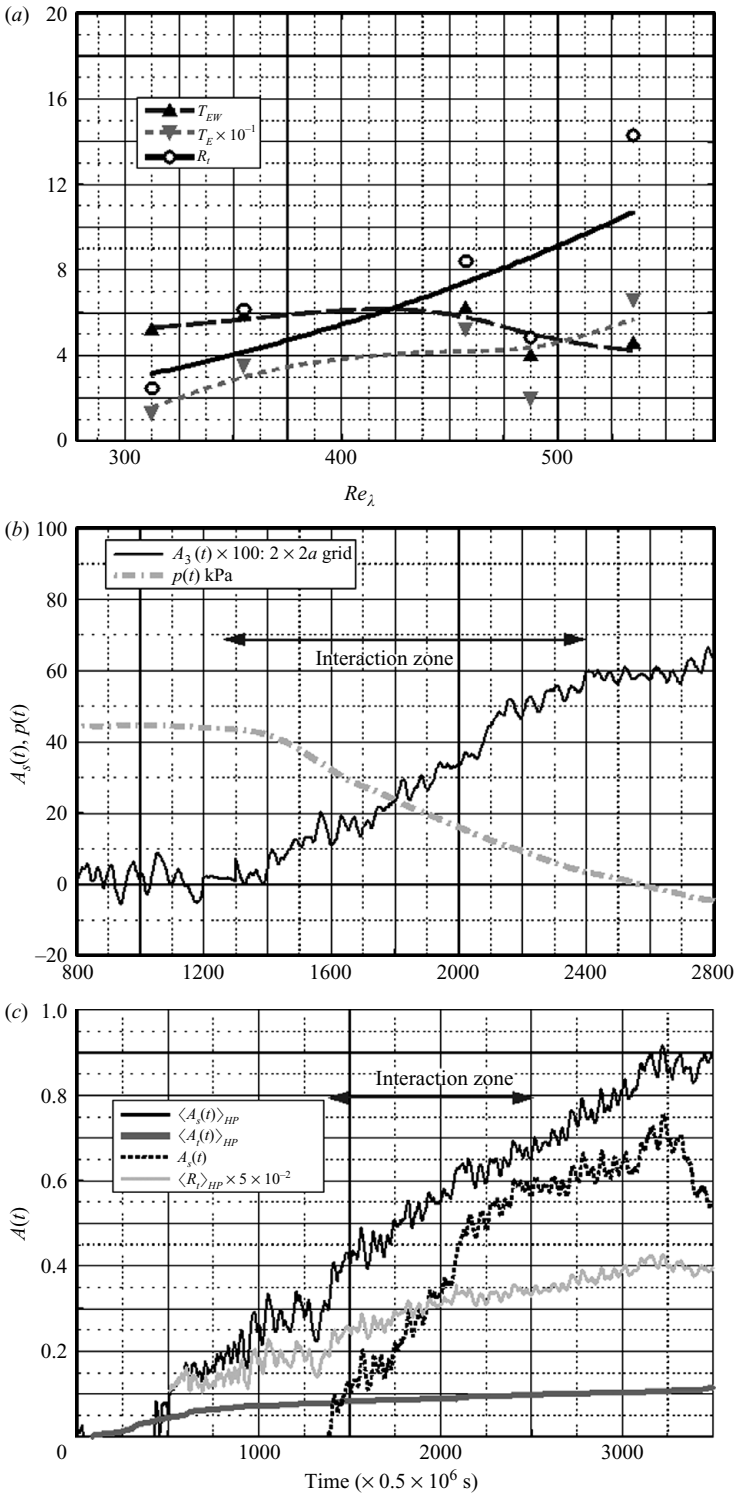

FIGURE 12. (*a*) Time scales of interaction T_{EW}, incoming turbulence T_ε and their ratio $R_t = T_\varepsilon / T_{EW}$ in various interactions. (*b*) Typical accumulative straining, $A_s(t)$ and pressure, $p(t)$ in the interaction for the $2 \times 2a$ grid. (*c*) Typical accumulative normalized straining, $\langle A_s(t) \rangle_{HP}$, and time of turbulence $\langle A_t(t) \rangle_{HP}$ and their ratio $\langle R_t(t) \rangle$ in the interaction. $A_s(t)$ has been shifted.

to fluctuations in S_{11} have no effect on A_s and possibly on the final state of turbulence after the interaction.

The cumulative effects of the normalized time of turbulence are expressed by the integral

$$\langle A_t(t)\rangle_{HP} = \int_{t_0}^{t} \frac{\langle E(t')\rangle_{HP}}{\langle 1/2U_i(t')U_i(t')\rangle_{HP}}\,\mathrm{d}t'$$

which involves the HP components only since they reasonably represent the true turbulent kinetic energy q^2 and its dissipation rate ε. Similarly, the integrated straining effect can be evaluated as

$$\langle A_s(t)\rangle_{HP} = \int_{t_0}^{t} \langle S_{11}(t')\rangle\,\mathrm{d}t'$$

along with the ratio $R_t(t) = \langle A_s(t)\rangle_{HP}/\langle A_t(t)\rangle_{HP}$. The results are plotted in figure 12(*c*).

The growth rate of these two quantities appears to be different, with the turbulent time scale increasing at a much slower rate than the straining time. Their ratio $\langle R_t(t)\rangle$ reaches values close to 6 in the upstream region and 8 downstream of the interaction region. These values agree well with the time-averaged values shown in figure 12(*a*). In figure 12(*c*), the values of the total instantaneous normalized straining time A_s are also plotted for comparison with its HP filtered part. The values of A_s are shifted in comparison with $\langle A_s(t)\rangle_{HP}$ because of the different starting time of integration. In the case of A_s, it starts at the beginning of the interaction. The rate of growth of A_s is higher than its HP component because there is a substantial LP component present in the total A_s.

8. Total enthalpy

The transport equation of the total energy per unit mass, $E_t = e + 1/2U_iU_i$ for flows without external forces and heat addition or subtraction is given by

$$\rho\frac{\mathrm{D}E_t}{\mathrm{D}t} = -\frac{\partial(pU_i)}{\partial x_i} + \frac{\partial(\tau_{ij}U_i)}{\partial x_j}, \tag{8.1}$$

where e is the internal energy per unit mass and τ_{ij} is the stress tensor equal to $2\mu S_{ij} + \lambda\delta_{ij}\ S_{kk}$ where λ is the second coefficient of viscosity. A similar transport equation for the total enthalpy per unit mass, $h_0 = E_t + p/\rho$, can be obtained as

$$\rho\frac{\mathrm{D}h_0}{\mathrm{D}t} = \frac{\partial p}{\partial t} + \frac{\partial(\tau_{ij}U_i)}{\partial x_j} = \frac{\partial p}{\partial t} + U_i\frac{\partial \tau_{ij}}{\partial x_j} + \tau_{ij}\frac{\partial U_i}{\partial x_j}, \tag{8.2}$$

where the last term on the right-hand side is the dissipation rate of kinetic energy $1/2U_iU_i$, with

$$E = \tau_{ij}\partial U_i/\partial x_j = \tau_{ij}S_{ij}.$$

The physical insights of this equation are obvious. The rate of change of the total enthalpy is provided by the rate of change of static pressure and the rate of work done by the viscous forces. It is also evident that even in the case of inviscid flows, h_0 is not constant in time-dependent flows. Figure 13(*a*) shows the measured values of total temperature, T_0, which is proportional to h_0, obtained in the experiments with the $2 \times 2a$ grid. Substantial reduction in T_0 can be observed in the interaction area of the expansion zone, whereas it remains relatively constant in the region upstream and downstream of it. It is also evident from these data that most of the drop in

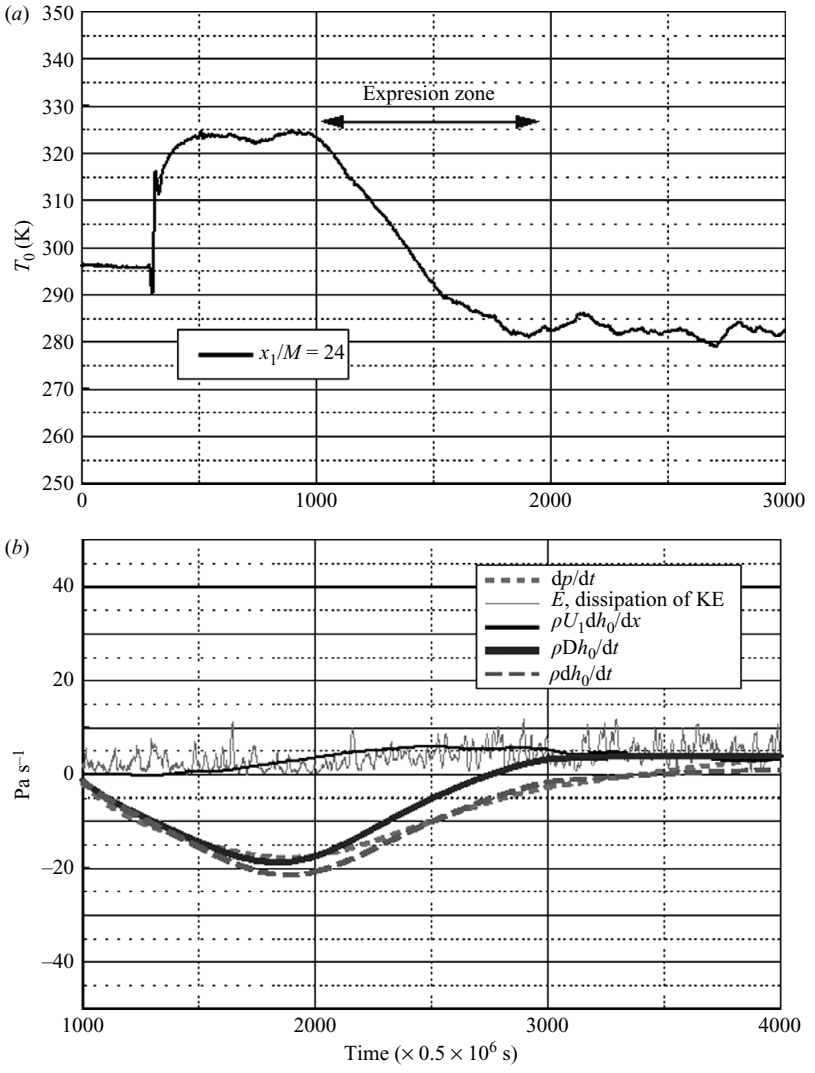

FIGURE 13. (*a*) Total temperature profile in the case of the $2 \times 2a$ grid. (*b*) Estimated values of the terms appearing in the transport equation of total enthalpy h_0. Dissipation data are amplified by a factor of 10 in relation to the other.

T_0 occurs at the beginning of the expansion zone which is expected from (8.2), and correlates well with the temporal pressure gradients shown in figure 7(*a*).

In order to explore further the role of (8.2), each of its terms has been estimated by using the data obtained here. The data obtained by the cross-wires at different longitudinal locations were used to obtain a fairly accurate measure of the convective term $\rho U_1 \partial h_0/\partial x_1$ while the dissipation rate of kinetic energy E, has been provided by the vorticity probe data. It was not possible to estimate the viscous term $U_i \partial \tau_{ij}/\partial x_j$.

The results are shown in figure 13(*b*). All the data have been smoothed out for clarity with exception of the dissipation rate, E. The term $\rho \partial h_0/\partial t$, which has been independently obtained through time-differentiation of the total temperature data, closely follows the behaviour of the pressure derivative term, $\partial p/\partial$t which has been obtained by differentiating the pressure transducer data. These are the two dominant

terms in the beginning of the expansion. The convective term $\rho U_1 \partial h_0/\partial x_1$ is small at the beginning of the interaction and upstream of it and grows slowly later on. It remains always positive even when the other terms have negative values. At the end of the interaction, $\partial p/\partial t$ diminishes, while $\rho \mathrm{D}h_0/\mathrm{D}t$ becomes positive, since it is mostly provided by the convective term $\rho U_1 \partial h_0/\partial x_1$. Downstream of the interaction zone, this term is solely balanced by the dissipation term and the viscous term $U_i \partial \tau_{ij}/\partial x_j$. The fact that the term $\rho U_1 \partial h_0/\partial x_1$ is positive may explain why the furthest downstream longitudinal velocity profiles are slightly higher than those close to the grid where the dissipation rate E is also high.

9. Turbulence modification through the interaction with expansion waves

Attenuation of turbulence is one of the major features of the outcome of the application of a longitudinal straining on isotropic turbulence. Linear analysis is expected to predict attenuation of turbulence as long as fluctuations of pressure, velocity and temperature upstream of the expansion waves are small so that the front is not substantially distorted.

Typically, the attenuation of turbulent fluctuations should depend on the expansion wave strength during the straining, the state of turbulence of the incoming flow before the interaction, and its level of compressibility.

Figure 14(a) shows the amplification/attenuation ratio, G, of the velocity vector fluctuations defined as the ratio of the standard deviation of the fluctuations downstream of the interaction σ_d to that upstream of the interaction σ_u, i.e. $G = \sigma_d/\sigma_u$. Data available from the two velocity components of various experiments obtained by X-wires and the wall pressure are plotted against the normalized distance from the grid, x/M, where M is the mesh size.

The data of the 8×8 grid case, which are shown in figure 14(a), indicate attenuation of longitudinal velocity fluctuations at all locations downstream of the grid. This attenuation is not the same at different locations from the grid. It appears that turbulence is most attenuated at the last measuring location where values of G close to 0.5 can be observed.

Fluctuations of the lateral velocity component are little affected by the straining and the interaction whereas pressure fluctuations at the wall show an attenuation of about 50 % which does not change with downstream distance.

In an effort to find out how turbulent length scales are affected by the longitudinal straining action, the longitudinal integral length scale L_{11} has been computed from the experimental data of the auto-correlation functions of the longitudinal velocity fluctuations, R_{11} after invoking Taylor's hypothesis. Thus, with $\overline{U}_1 = \xi_1 \tau$ it appears that

$$L_{11}(x_1) = \int_0^\infty R_{11}(x_1, \xi_1)\, \mathrm{d}\xi_1 = \overline{U}_1 \int_0^\infty R_{11}(x_1, \tau)\, \mathrm{d}\tau.$$

Typical data of the ratio $G_{L11} = L_{11,d}(\xi_1)/L_{11,u}(\xi_1)$ plotted against x_1/M are also shown in figure 14(a). The data clearly show that the integral length scales are amplified considerably through the interaction, as is expected. Most of this amplification, however, is due to the increased ratio of the mean velocities U_{1d}/U_{1u} because of the flow acceleration during the straining.

Attenuation of longitudinal fluctuations through the whole flow field have also been observed in the case of the 4×4 grid (see figure 14b). Lateral velocity fluctuations are attenuated close to the grid and amplified further downstream. The data obtained with the vorticity probe seem to fit this pattern. The attenuation data presented

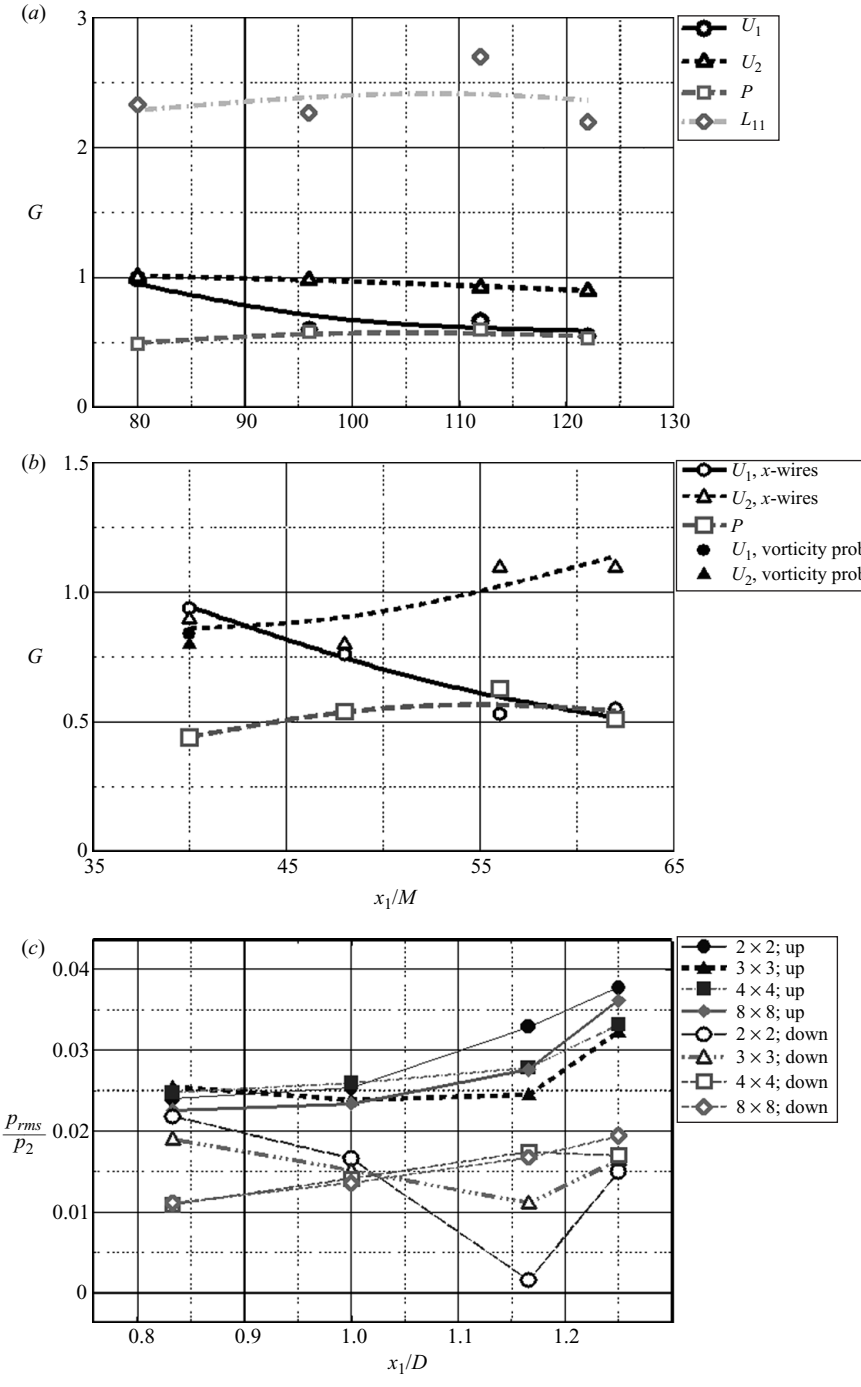

FIGURE 14. (*a*) Amplifications/attenuation of turbulent fluctuations and integral length scales downstream of the grid in the case of the 8×8 grid. (*b*) Amplifications/attenuation of turbulent fluctuations downstream of grid in the case of the 4×4 grid. (*c*) Wall pressure fluctuations before and after the interaction. Filled symbols before, and open symbols after the interaction.

here have been obtained in incoming flows, which are practically incompressible since the Mach number is slightly below 0.3. The passage of the expansion waves, however, accelerates the flow to Mach numbers of about 0.5 or more. Thus, during the interaction, compressibility effects start to play a significant role and therefore it is expected to affect the flow development. The data in figure 14(*b*) also show a reasonably good agreement between the data obtained with the X-wires and those with the vorticity probe. Pressure fluctuations seem to be attenuated substantially throughout the whole flow field.

These wall pressure fluctuations are mostly the result of turbulence within the wall boundary layer whereas the isotropic turbulence which acts as a free-stream turbulence to the boundary layer has a secondary effect. In that respect, scaling with the shock tube diameter D may be more appropriate than the mesh size M. These data are re-plotted in figure 14(*c*). These pressure fluctuations are related to the local shear stress. In fact, Willmarth & Wooldridge (1962) and Andreopoulos & Agui (1996) found that the r.m.s. of pressure fluctuations is about twice the local wall stress. The presence of free-stream turbulence increases the local skin friction slightly and, therefore, the wall pressure fluctuations (Hancock & Bradshaw 1989). The data in figure 14(*c*) suggest that the shear stress is higher at larger distances from the grid before the interaction. This agrees with the notion that wall shear stress is higher at locations closer to the origin of the unsteady boundary layer that is associated with the shock foot. After the interaction, wall shear stress is significantly reduced because of damped turbulent activities.

Figure 15(*a*) shows the ratios of the standard deviations, $G = \sigma_d/\sigma_u$ for the longitudinal and lateral velocity and vorticity fluctuations as a function of the characteristic time scale, L_ε/q, of the incoming turbulence. In addition to the locations where vorticity measurements were carried out, some typical data obtained with X-wire probes in several locations away from the grid were also plotted in the same figure. To avoid overwhelming data information, only three data points of longitudinal velocity fluctuations are plotted for each of the grids. For the 8×8 grid for instance, the mid-flow-field point has a value of $L_\varepsilon/q = 12.94$ m s whereas its first measuring point corresponds to $L_\varepsilon/q = 10.2$ m s and its last measuring point to $L_\varepsilon/q = 15.3$ m s. The corresponding values of G are between 1 and 0.6 with 0.8 the value at the mid-field point.

The data of longitudinal velocity fluctuations clearly demonstrate that in addition to L_ε/q, G also depends on the particular grid used to generate the turbulent field. Attenuation increases with increasing time scale within each of the flows generated by the grids used in the present investigation. Fine grids are characterized by small time scales and they attenuate velocity fluctuations more than coarse grids where time scales are greater. The data shown above indicate that amplification depends on the time scale of the incoming turbulence and on the grid, which suggests that the state of the incoming turbulence affects amplification or attenuation.

It appears that lateral vorticity fluctuations attenuated the most with ratios between 0.74 and 0.42. The data also show that the attenuation is stronger in fine grids with small time scales. Longitudinal vorticity fluctuations show, on average, a slight amplification throughout the investigated range of L_ε/q. Lateral velocity fluctuations appear to be unaffected by the applied expansive straining.

In order to investigate the effect of the strength of the applied straining on amplification/attenuation of turbulent fluctuations, the data of G have been plotted in figure 15(*b*) against non-dimensional time R_t. The data clearly indicate that there is an attenuation of longitudinal velocity fluctuations in all cases which becomes

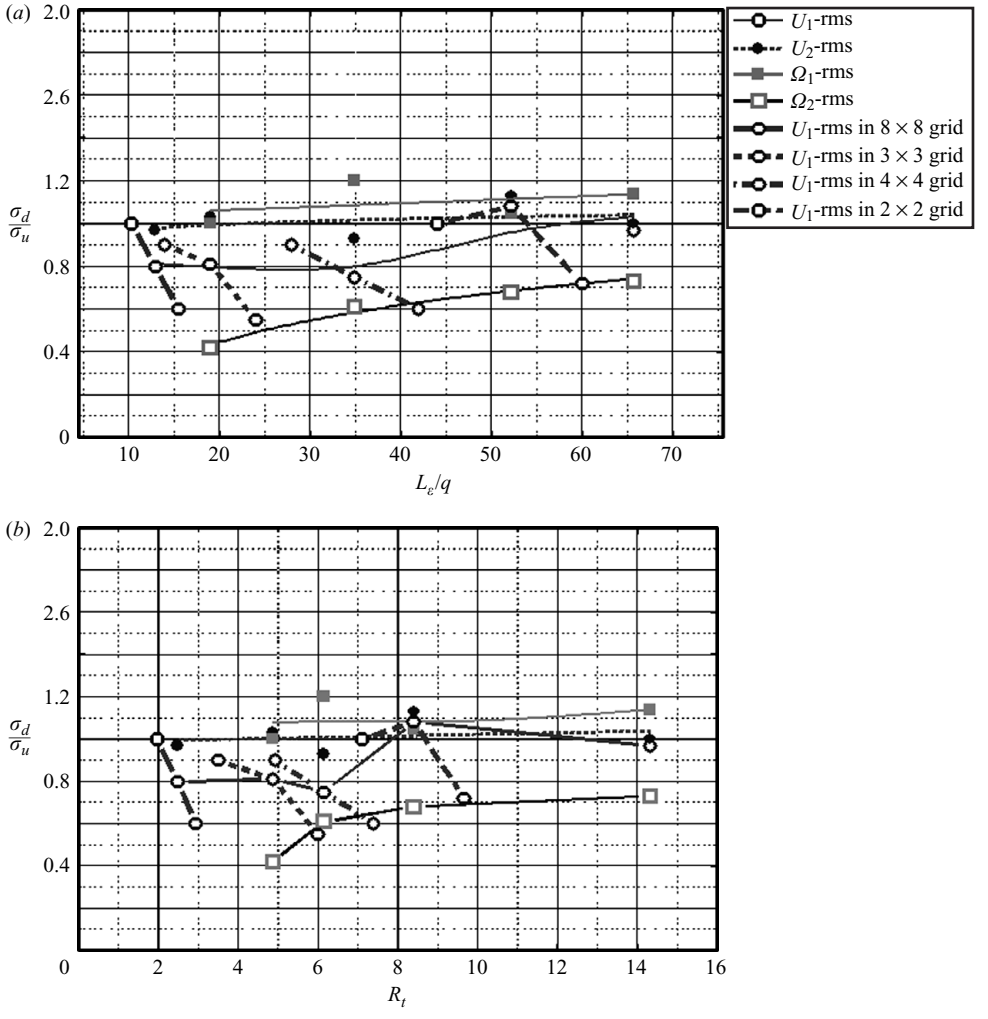

FIGURE 15. (*a*) Attenuation of velocity and vorticity fluctuations in expansion wave interactions with turbulence as a function of its time scale L_ε/q. (*b*) Attenuation of velocity and vorticity fluctuations in expansion wave interactions with turbulence as a function of non-dimensional time S_t.

stronger with increasing R_t within the same grid generated flow. Attenuation at a fixed R_t is not uniquely defined and it depends on the grid. This suggests that the state of turbulence as defined by its characteristic quantities plays a substantial role in the outcome of the present interactions. One parameter such as L_ε/q or R_t is not enough to characterize the interactions.

The results in figure 15(*b*) also demonstrate that substantial attenuations take place within a shorter time R_t in fine grids than in coarse grids. In the case of the 8×8 grid, for instance, attenuation of 0.4 occurs within 1 non-dimensional time unit whereas in the case of the 2×2 grid, attenuation of 0.28 ($G = 0.72$) takes places after $\Delta S_t = 2.7$.

Even in cases with short R_t, where the interactions are not rapid and therefore RDT may not be applicable, attenuation of turbulent fluctuations has been predicted. Ribner & Tucker (1953) investigated the case of isotropic turbulence through a

contraction by assuming that turbulence can be represented by a superposition of planar waves, and by considering the incoming state of turbulence, predicted the change in the spectral densities as a function of the contracting length ratios in the three directions. The decay of turbulence within the contraction was taken into account through a correction function and the streamline curvature within the contraction which stabilizes turbulence was not considered explicitly. For volumetric ratios $J = \overline{\rho}_d/\overline{\rho}_u$ between 0.75 and 0.88, values of the predicted gain, G, in longitudinal velocity r.m.s. were between 0.5 and 0.8. Given that these values include viscous corrections provided by an empirical decay relation, their agreement with the measured values is reasonably good.

10. Spectral densities

Some further insight into the evolution of turbulence through the expansion waves can be obtained by looking into the one-dimensional frequency spectra (power spectral densities) of each of the three vorticity components. It is more meaningful to consider the high-pass filtered part of the signals rather than the low-pass ones. Conservation laws and RDT in the present case are usually considered on a moving frame of reference associated with the travelling expansion waves which propagate with the local speed of sound relative to the upstream flow, C_u. In the context of RDT, the wavenumber will be reduced by interaction by the volumetric ratio J and the velocity will increase by J^{-1}. Thus, it appears that the downstream wavenumber will be $k_d = Jk_u$ and $C_d = J^{-1}\,C_u$. If we consider a representative longitudinal wave which has the form $\exp(k_u x_1)$ at a point upstream of the interaction and $\exp(k_d x_1')$ downstream of the interaction, then $\mathrm{k}_u x_1 = k_u C_u t$ and $k_d x_1' = k_d C_d t$. By substituting the relations between upstream downstream values of k and C, it can be shown that $k_d C_d = Jk_u J^{-1} C_u = k_u C_u$. Thus, the temporal frequency f does not change through the interaction and it is $f = k_u C_u/2\pi = C_u/\lambda_u = k_d C_d/2\pi = C_d/\lambda_d$ in both cases. In that respect, the present changes in the spectral densities will be considered at constant frequency f.

Figure 16(a) shows the frequency spectra of the vorticity components Ω_1, Ω_2 and Ω_3 upstream and downstream of the interaction obtained in the flow with the $2 \times 2a$ grid. The upper limit in the wavenumber scales is defined by the temporal resolution of the instrumentation and the lower limit is associated with cutoff frequency of the high-pass filtering which corresponds to large eddies with size of the order of the shock tube diameter D. For instance, for $D = 0.3\,\mathrm{m}$ $C_u/D = 1216\,\mathrm{Hz}$. For the size of the vorticity probe $l_p = 1.3\,\mathrm{mm}$, $C_u/l_p = 280\,\mathrm{kHz}$. However, if $U_u = 100\,\mathrm{m\,s^{-1}}$ is used, then the time scales at error start above 100 kHz. The location of the maximum value which is associated with the most energetic eddies appears to be between 10 and 15 kHz, which corresponds to wavelengths between $\lambda \approx 2$ and 2.4 mesh sizes M. The interaction slightly shifts the spectral content of the two lateral vorticity components towards higher frequencies. There is also attenuation of their amplitude in frequencies greater than about 8 kHz. The amount of attenuation across the wavenumber spectrum has been further explored by considering the ratio of the corresponding spectral densities before and after the interaction at the same frequency, $\langle G(f)\rangle_{HP} = \langle f\Phi_d(f)\rangle_{HP}/\langle f\Phi_u(f))\rangle_{HP}$. Values of $\langle G(f)\rangle_{HP}$ corresponding to the data of figure 16(a) are shown in figure 16(b). There is a variation of $\langle G(f)\rangle_{HP}$ across the spectrum. Significant attenuation in the spectral content of the lateral vorticity components of the data occurs at frequencies $f > 8\,\mathrm{kHz}$ with a maximum in the range $40\,\mathrm{kHz} < f < 60\,\mathrm{kHz}$. In terms of wave length λ_u, this range corresponds

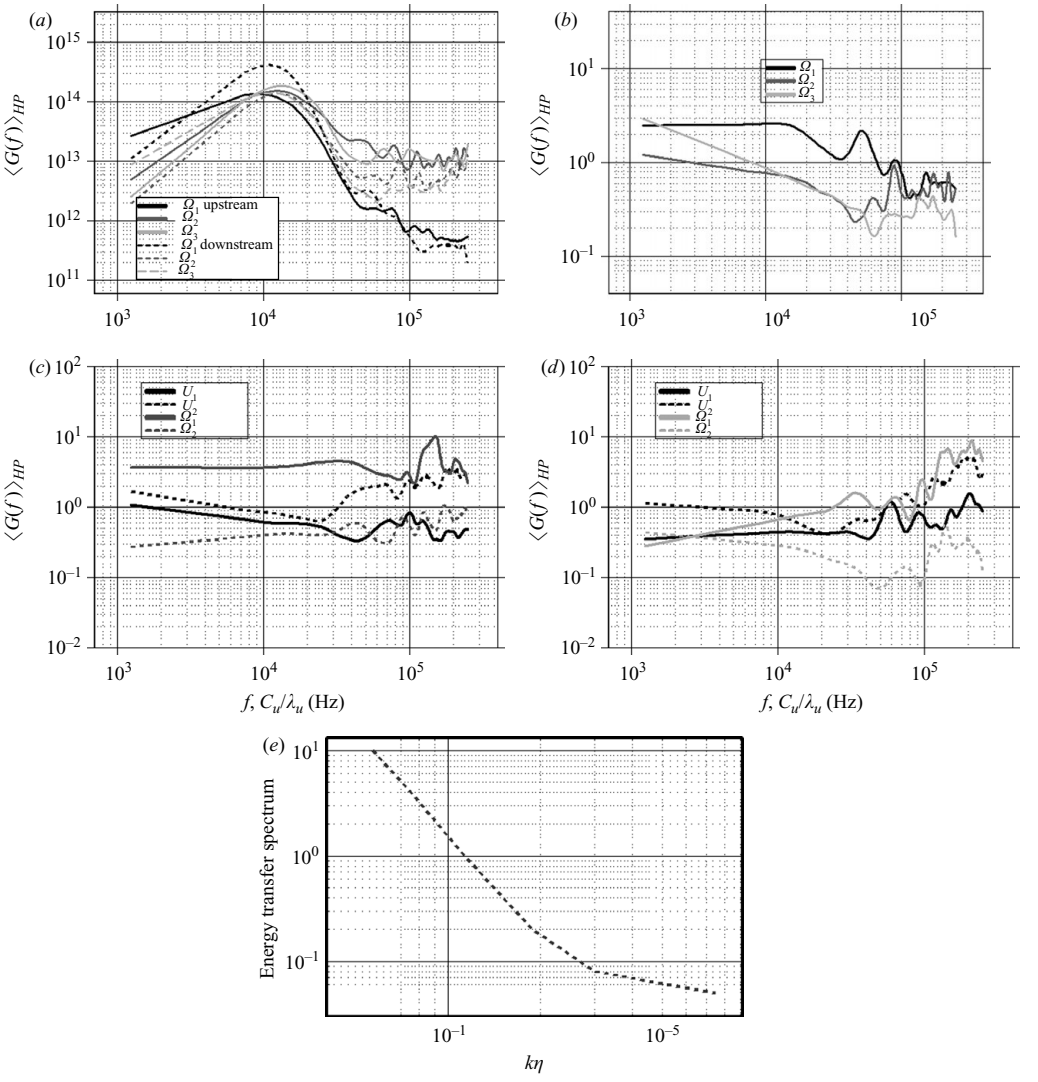

FIGURE 16. (*a*) Frequency-weighted power spectral densities of the high-pass filtered signals of the three vorticity components in the case of $2 \times 2a$ grid. (*b*) Ratio of frequency-weighted power spectral densities of vorticity component fluctuations before and after the interaction in the case with the $2 \times 2a$ grid. (*c*) Ratio of frequency-weighted power spectral densities of velocity and vorticity component fluctuations before and after the interaction in the case with the 4×4 grid. (*d*) Ratio of frequency-weighted power spectral densities of velocity and vorticity component fluctuations before and after the interaction in the case with the 3×3 grid. (*e*) Energy transfer spectrum $\hat{T}(k)$ in the case of $2 \times 2a$ grid.

to $0.40 < \lambda/M < 0.71$. If this range is compared to the most energetic eddy size of $\lambda/M = 2$, then we can conclude that most of the attenuation process takes place in eddies with sizes of a fraction of the energetic ones.

Both graphs in figure 16(*b*) indicate some amplification of the fluctuations at some low frequencies with $f < 8\,\text{kHz}$ which corresponds to $\lambda/M > 3.6$. Amplification of longitudinal vorticity fluctuations is observed in all frequencies below 40 kHz.

Grid	Mesh size M (mm)	Most energetic frequency (kHz)		Most energetic λ/M		Most attenuating frequency (kHz)		Most attenuating λ/M	
		U_1	Ω_2	U_1	Ω_2	U_1	Ω_2	U_1	Ω_2
$2\times 2a$	12.7	9	10.5	3.19	2.75	<2.5	60	>10	0.5
3×3	8.5	9	10.4	4.77	4.12	30	50	> 1	0.86
4×4	6.35	8	10.2	7.10	5.6	40	65	1.43	0.88

TABLE 5. Summary of energetics.

Values of the vorticity and velocity fluctuations ratio $\langle G(f)\rangle_{HP}$ for the case of the 4×4 grid with mesh size $M=6.35$ mm are shown in figure 16(c). Substantial attenuation of longitudinal velocity fluctuations can be observed through the whole range of frequency while the lateral velocity fluctuations show moderate attenuation in the range of $\lambda/M>2$ and $\lambda/M<11.5$. Longitudinal vorticity fluctuations are amplified and lateral vorticity fluctuations are attenuated significantly throughout the frequency range. The data for the 3×3 grid exhibit a significant attenuation of both vorticity and velocity fluctuations of all components in the range of $0.75<\lambda/M<1.57$. The degree of attenuation of lateral vorticity fluctuations appears to be higher in the present case of a finer grid. There is also some evidence of rather low amplification of lateral velocity fluctuations and longitudinal vorticity fluctuations in the wavelength ranges of the spectra for $\lambda/M>0.75$.

A summary of the findings of the spectral analysis is shown in table 5. The location of the maximum amplitude which is considered as the most energetic frequency shifts slightly to higher frequency in the cases of vorticity fluctuations than in the cases of velocity fluctuations. In terms of normalized wavelength λ/M, it appears that the maximum spectral content in the cases of vorticity fluctuations occurs at shorter wavelengths than the peak in the velocity spectra. One other characteristic of vorticity is that eddies with sizes of a fraction of the energy-containing eddies attenuate the most.

The dynamics of turbulence can be further explored by considering the transfer of energy from larger to smaller eddies and the interactions among the Fourier modes. Of particular interest is the evolution of kinetic energy of the Fourier mode defined as $\hat{E}(k)=1/2|\hat{u}_i^*(k)\hat{u}_i(k)|$ where $\hat{u}_i(k)$ is the Fourier transform of the velocity component u_i and $*$ denotes a complex conjugate. The evolution equation for $\hat{E}(k)$ in incompressible isotropic flows according to Pope (2000) has the form

$$\partial\hat{E}(k)/\partial t=\hat{T}(k)-\hat{D}(k),$$

where $\hat{T}(k)$ represents the energy transfer between modes, and $\hat{D}(k)=2\nu k^2\hat{E}(k)$ is related to the dissipation spectral density. When the above equation is summed over all wavenumbers k, its left-hand side is $\mathrm{d}q/\mathrm{d}t$ and the last term in the right-hand side is the dissipation rate ε. The summation of $\hat{T}(k)$ over k is zero because the various contributions of energy transfer between the modes cancel out. Then, it appears that $\mathrm{d}q/\mathrm{d}t=-\varepsilon$ which is the classical relation of the turbulent kinetic energy decay for isotropic turbulence. According to Domaradzki (1992), $\hat{T}(k)$ is totally balanced by $\hat{D}(k)$ at wavenumbers beyond those at the energy containing range. Thus, $\hat{T}(k)\approx\hat{D}(k)$ and therefore the dissipation spectrum can provide information on the energy transfer $\hat{T}(k)$. The present flow is considered weakly compressible and the dilatational dissipation $\varepsilon_d=4/3S_{kk}S_{kk}$ is about 8 % of the total dissipation

ε. Thus, it appears that the dissipation rate can be approximated by $\varepsilon \approx \nu \Omega_i \Omega_i$. Since $k^2 \hat{E}(k) = 1/2 \hat{\Omega}_i(k) \hat{\Omega}_i(k)$ then it follows that $\hat{D}(k) = \nu \hat{\Omega}_i(k) \hat{\Omega}_i(k)$. Therefore, by summing up the individual spectral densities of the three vorticity components shown in figure 16(*a*), we can obtain information about the energy transfer $\hat{T}(k)$. The validity of the present assumptions is in the range of frequencies greater than 18 kHz which corresponds to $k\eta > 0.06$. The data are re-plotted in figure 16(*e*) and they clearly suggest that $\hat{T}(k)$ is nonlinear with $k\eta$. In the range of $k\eta$ between 0.06 and 0.3, the results show an exponential decay of $\hat{T}(k) \sim \exp(-\alpha k)$ with an estimated value of $\alpha = 7.5\eta$ fitting the present data obtained at $Re_\lambda = 488$. After the interaction, the data show a larger exponential decay, possibly because of processes related to the return to isotropy.

11. Conclusions

The effects of straining and the associated bulk dilatation provided by a set of moving expansion waves on isotropic turbulence have been investigated experimentally. The present flow configuration does not involve any streamline curvature as in the cases of expansion around corners.

Flows with Reynolds numbers based on Taylor's microscale ranging from 310 to 488 have been configured. The flow fields have been investigated by measuring the three-dimensional velocity and vorticity vectors, the full velocity gradient and rate-of-strain tensors with instrumentation of high temporal and spatial resolution. This provided estimates of dilatation, compressible dissipation and dilatational stretching to be obtained.

The relatively long duration of the straining region of the expansion zone allowed for a temporally and spatially resolved analysis of all the quantities obtained by decomposing all the signals into their low- and high-frequency contents.

Although the average value of the applied straining was between $S_{11} = 160\,\mathrm{s}^{-1}$ and $250\,\mathrm{s}^{-1}$, the flow accelerated from a Mach number of 0.23 to about 0.56, a value which is more than twice the initial one. Amplitude of fluctuations of the strain rate S_{11} were of the order of $4000\,\mathrm{s}^{-1}$ before the application of straining, and reduced by about 2.5 times downstream of the interaction. One of the most remarkable features of the suppression of the turbulence is that this process peaks shortly after the application of the straining where the pressure gradient has a minimum. It was also found that the total enthalpy variation closely follows the temporal gradient of pressure within the straining region and peaks at the same location as the pressure gradient.

The present results indicate that the outcome of the interaction depends strongly on the upstream turbulence of the flow which has been generated by each individual grid. Longitudinal velocity fluctuations have been observed to attenuate in all experiments at large times. The results have shown that attenuation within a given grid flow increases with time and distance from the grid which also suggests that attenuation increases with increasing Reynolds number, because Re_λ also increases with distance or time. The data of velocity fluctuations in the lateral directions show no consistent behaviour change or some minor attenuation through the interaction.

Spectral analysis has indicated that attenuation of fluctuations is not the same across all wavenumbers of the spectrum. The magnitude of attenuation appears to be higher in cases of finer mesh grids.

Vorticity fluctuations of the lateral components were attenuated substantially more than the longitudinal velocity fluctuations. There is evidence suggesting that their attenuation increases with increasing Re_λ. Analysis of the spectral content of

these fluctuations indicated that their attenuation also depends on the wavenumber. Although it is expected that most of the impact of the interaction will be felt on the high-wavenumber part of the vorticity spectra since most of the vorticity fluctuations originate from small scales, the attenuation peaks at mid-range wavenumbers and continues at high wavenumbers. Fluctuations of vorticity in the longitudinal direction are affected considerably less than those in the lateral direction by the applied straining.

The financial support provided by NASA Grant NAG3-2163 and AFOSR Grant F49620-98-20358 is greatly acknowledged.

REFERENCES

Agui, J. H. 1998 *Shock Wave Interactions with Turbulence and Vortices*. PhD thesis. The City University of New York.

Agui, J. H. & Andreopoulos, Y. 2003 A new laser vorticity probe – LAVOR: its development and validation in a turbulent boundary layer. *Exps. Fluids* **34**, 192–205.

Agui, J. H., Briassulis, G. & Andreopoulos, Y. 2005 Studies of interactions of a propagating shock wave with decaying grid turbulence: velocity and vorticity field. *J. Fluid Mech.* **524**, 143–195.

Andreopoulos, J. & Agui, J. 1996 Wall vorticity flux dynamics in a two-dimensional turbulent boundary layer. *J. Fluid Mech.* **309**, 45–84.

Andreopoulos, Y. & Honkan, A. 2001 An experimental study of the dissipative and vortical motions in turbulent boundary layers. *J. Fluid Mech.* **439**, 131–163.

Andreopoulos, Y., Agui, J. H. & Briassulis, G. 2000 Shock wave-turbulence interactions. *Annu. Rev. Fluid Mech.* **32**, 309–345.

Arnette, S. A., Samimy, M. & Elliott, G. S. 1995 Structure of supersonic turbulent boundary layer after expansion regions. *AIAA J.* **33**, 430–438.

Batchelor, G. K. & Townsend, A. A. 1947 Decay of vorticity in isotropic turbulence. *Proc. R. Soc. Lond.* A **199**, 238–255.

Bendat, J. S. & Piersol, A. G. 2000 *Random Data Analysis and Measurements Procedures*. Wiley.

Briassulis, G., Honkan, A., Andreopoulos, J. & Watkins, B. C. 1995 Applications of hot-wire anemometry in shock tube flows. *Exps. Fluids.* **19**, 29–37.

Briassulis, G., Agui, J. & Andreopoulos, Y. 2001 The structure of weakly compressible grid turbulence. *J. Fluid Mech.* **432**, 219–283.

Dawson, J. D., Samimy, M. & Amette, S. A. 1994 The effects of expansion on a supersonic boundary layer: surface pressure measurements. *AIAA J.* **32**, 2169–2177.

Domaradzki, J. A. 1992 Nonlocal triad interactions and the dissipation range of isotropic turbulence. *Phys. Fluids* A **4** (9), 2037–2045.

Dussauge, J. P. & Gaviglio, J. 1987 The rapid expansion of a supersonic turbulent flow: role of bulk dilatation. *J. Fluid Mech.* **174**, 81–112.

Johnson, A. W. 1993 Laminarization and retransition of turbulent boundary layers in supersonic flow. PhD dissertation, Yale University, New Haven, CT.

Hancock, P. E. & Bradshaw, P. 1989 Turbulence structure of a boundary layer beneath a turbulent free stream. *J. Fluid Mech.* **205**, 45–63.

Honkan, A. & Andreopoulos, Y. 1997*a* Vorticity, strain-rate and dissipation characteristics in the near-wall region of turbulent boundary layers. *J. Fluid Mech.* **350**, 29–96.

Honkan, A. & Andreopoulos, Y. 1997*b* Instantaneous three dimensional vorticity measurements in vortical flow over a delta wing. *AIAA J.* **35**, 1612–1620.

Hunt, J. R. C. 1973 A theory of turbulent flow round two-dimensional bluff bodies. *J. Fluid Mech.* **61**, 625–636.

Morkovin, M. V. 1955 Effects of high acceleration on a turbulent supersonic shear layer. Proceedings, Heat Transfer and Fluid Mechanics Institute, Los Angeles, California.

Morkovin, M. V. 1960 Note on assessment of flow disturbances at a blunt body traveling at supersonic speeds owing to flow disturbances in free stream. *J. Appl. Mech.* **27**, 223–229.

NARASHIMA, R. & SREENIVASAN, K. R. 1973 Relaminarization in highly accelerated turbulent boundary layers. *J. Fluid Mech.* **61**, 417–447.

NARASHIMA, R. & VISWANATH, P. R. 1975 Reverse transition at an expansion corner in supersonic flow. *AIAA J.* 693–695.

POPE, S. B. 2000 *Turbulent Flows*. Cambridge University Press.

RIBNER, H. S. & TUCKER, M. 1953 Spectrum of turbulence in a contracting stream. *NACA TN* 1113.

ROE, P. L. 1981 Approximate Riemann solvers, parameter vectors, and difference schemes. *J. Comput. Phys.* **43**, 357–372.

SMITH, D. R. & SMITS, A. J. 1991 The rapid expansion of a turbulent boundary layer in a supersonic flow. *Theoret. Comput. Fluid Dyn.* **2**, 319–328.

STERNBERG, J. 1954 The transition from a turbulent to a laminar boundary layer. Rep. 906, May, Ballistic Research Labs., Aberdeen.

VIVEKANANDAN, R. 1963 A study of boundary layer expansion fan interactions near a sharp corner in supersonic flow. MSc thesis, Dept of Aeronautical Engineering, Indian Institute of Science, Bangalore, India.

VISWANATH, P. R. & NARASHIMA, R. 1973 Base pressure on sharply boat-tailed aft bodies. Rep. 72 FMI, July, Dept of Aeronautical Engineering, Indian Institute of Science, Bangalore, India.

WILLMARTH, W. W. & WOOLDRIDGE, C. E. 1962 Measurements of the fluctuating pressure at the wall beneath a thick boundary layer. *J. Fluid Mech.* **14**, 187–196.